

Time-Dependent Models for Blazar Emissions with the Second-Order Fermi Acceleration

KATSUAKI ASANO¹, FUMIO TAKAHARA², MASAOKI KUSUNOSE³, KENJI TOMA², AND JUN KAKUWA⁴

asanok@icrr.u-tokyo.ac.jp

Submitted; accepted

ABSTRACT

The second order Fermi acceleration (Fermi-II) driven by turbulences may be responsible for the electron acceleration in blazar jets. We test this model with time-dependent simulations. The hard electron spectrum predicted by the Fermi-II process agrees with the hard photon spectrum of 1ES 1101-232. For other blazars that show softer spectra, the Fermi-II model requires radial evolutions of the electron injection rate and/or diffusion coefficient in the outflow. Such evolutions can yield a curved electron spectrum, which can reproduce the synchrotron spectrum of Mrk 421 from radio to X-ray. The photon spectrum in GeV energy range of Mrk 421 is hard to be fitted by synchrotron self-Compton model. However, if we introduce an external radio photon field with a luminosity of 4.9×10^{38} erg s⁻¹, GeV photons are successfully produced via inverse Compton scattering. The temporal variability of the diffusion coefficient or injection rate causes flare emission. The observed synchronicity of X-ray and TeV flares implies a decrease of the magnetic field in the flaring source region.

Subject headings: acceleration of particles — BL Lacertae objects: individual (1ES 1101-232, Mrk 421) — radiation mechanisms: non-thermal — turbulence

¹Institute for Cosmic Ray Research, The University of Tokyo, 5-1-5 Kashiwanoha, Kashiwa, Chiba 277-8582, Japan

²Department of Earth and Space Science, Osaka University, Osaka, 560-0043, Japan

³Department of Physics, School of Science and Technology, Kwansai Gakuin University, Sanda 669-1337, Japan

⁴Department of Physical Science, Hiroshima University, Higashi-Hiroshima, 739-8526, Japan

1. Introduction

Multifrequency spectra of blazars are characterized by the double peaks of the synchrotron and inverse Compton components. They have been successfully fitted by steady-state leptonic models (e.g. Kino, Takahara & Kusunose 2002; Celotti & Ghisellini 2008). In most models, non-thermal emissions are presumed to be emitted by shock accelerated electrons (Fermi-I process, e.g. Kirk et al. 1998; Spada et al. 2001). The flare phenomena may be caused by internal shocks in the blazar outflows as have been discussed in the models of the prompt emission of gamma-ray bursts (GRBs, Mészáros 2006).

However, the emissions from blazars, especially in quiescent states, can be regarded as quasi-steady differently from GRBs. The existence of the steady shocks in the outflows is nontrivial. This may imply a different acceleration process from the Fermi-I. The electron energy distributions obtained from the photon-spectrum fits also raise a doubt on the Fermi-I acceleration. The maximum energy of electrons is far below the Bohm limit (Inoue & Takahara 1996), while electrons accelerated by the shocks of supernova remnants attain energies close to the Bohm limit (Aharonian & Atoyan 1999; Yamazaki et al. 2004). The detections of very high-energy gamma-rays ($> 10^{11}$ eV) from high-redshift blazars (Aharonian et al. 2006, 2007a,b), despite obligate absorption due to extragalactic background light (EBL), indicate very hard photon spectra (photon index $\lesssim 1.5$). Those unusually hard spectra are reinforced by the non-detection of GeV photons with *Fermi* (Neronov & Vovk 2010). The implied electron spectra may be harder than the prediction of the simplest version of diffusive shock acceleration theory; the electron spectral index should be larger than 2. Several mechanisms to produce harder spectra for the shock accelerated particles have been proposed, though they are not well established yet. The nonlinear back reaction of cosmic-ray pressure on the shock structure (Malkov & Drury 2001) is frequently discussed. Alternatively, Vainio & Schlickeiser (1999) considered the particle acceleration in nonrelativistic shock and showed that the electron power-law spectral indices can be smaller than 2 when the scattering center compression ratio is larger than the gas compression ratio. Vainio, Virtanen & Schlickeiser (2003) also demonstrated this for relativistic shocks.

The second order Fermi acceleration (Fermi-II) is a promising process to make hard spectra (e.g. Schlickeiser 1984; Park & Petrosian 1995; Becker, Le & Dermer 2006; Stawarz & Petrosian 2008). This slow acceleration process can naturally explain the lower maximum energy of electrons. Applications of the Fermi-II to AGN jet emissions have been discussed by several authors (e.g. Böttcher, Pohl & Schlickeiser 1999; Schlickeiser & Dermer 2000; Katarzyński et al. 2006). The turbulences responsible for the Fermi-II acceleration may be induced by the Kelvin-Helmholtz instability (Hardee 2004; Mizuno, Hardee & Nishikawa 2007) or the current driven instability (Lyubarskii 1999; Narayan, Li & Tchekhovskoy 2009; Mizuno, Hardee & Nishikawa

2011). Such instabilities may be triggered by recollimation of the jet induced by a pressure gradient in the medium (Daly & Marscher 1988; Komissarov & Falle 1997; Agudo et al. 2001). Actually, the signature of the Fermi-II has been explored in photon spectra. X-ray spectra have been fitted with a curved function, such as the log-parabolic shape, which has been discussed in the theoretical context of the Fermi-II process (Massaro et al. 2004a,b; Tramacere et al. 2009). Even for GRBs, the Fermi-II process has been considered (Asano & Terasawa 2009) to yield hard spectra below the spectral peak energy ($\sim 0.1\text{--}1$ MeV).

Lefa, Rieger & Aharonian (2011) adopt the Fermi-II process to fit a hard blazar 1ES 0229+200, though their discussion focuses on the balance between the acceleration and cooling. In this paper we further pursue the possibility of the Fermi-II in blazar jets. Here we use the time-dependent code of Asano & Mészáros (2011) developed for GRB studies (see also Asano & Mészáros 2012) to follow the evolutions of the electron energy distribution and photon production. In our code, the electron distribution is obtained with the effects of the injection, acceleration, radiative cooling, adiabatic cooling, electron–positron pair production, and heating due to synchrotron self-absorption. Based on the photon production and escape from the source region, the code outputs photon spectra and lightcurves for an observer including the Doppler and curvature effects.

We try to fit the wide-band spectra of 1ES 1101-232 and Mrk 421 with our simulations. This would be the first application of comprehensive Fermi-II models to current data of wide-band blazar spectra with a time-dependent method.¹ Temporal evolutions of the electron and photon energy-distributions will be explicitly shown, which helps us understand the roles of the temporal evolutions of the Fermi-II process and particle injection rate on photon spectra. We will show that the temporal evolution is important not only for the spectral variability in flares (Kusunose, Takahara & Li 2000; Chen et al. 2011) but also for steady emissions. Temporal evolutions of injection rate and acceleration efficiency etc. may play an important role in steady photon spectra (see e.g., Becker, Le & Dermer 2006).

In §2, we explain our model and numerical method. The results for the hard spectrum blazar 1ES 1101-232 are shown in §3. The results for the famous blazar Mrk421 are divided into two parts: §4 for the steady photon spectrum and §5 for the spectral variability in flares. The summary and discussion are in §6. To provide spectra and lightcurves for an observer, we adopt the cosmological parameters $H_0 = 70 \text{ km s}^{-1} \text{ Mpc}^{-1}$, $\Omega = 0.3$, and $\Lambda = 0.7$.

¹ The main purpose of Lefa, Rieger & Aharonian (2011) is not to fit data, while they fit the TeV spectrum of 1ES 0229+200 with a peculiar model, a Maxwell-like electron distribution due to the balance between the acceleration and cooling. The time-dependent effects discussed there are not applied to the spectral fit.

2. Numerical Methods

Our model is summarized in Figure 1. The calculation starts at a radius $R = R_0$, where high-energy electrons also start to be injected. The quasi-steady outflow is modeled by identical shells continuously ejected from $R = R_0$. We consider a shell region of a constant width $W = R_0/\Gamma^2$ (R_0/Γ in the comoving frame) that is moving outward with Lorentz factor $\Gamma = 1/\sqrt{1 - \beta^2}$. Our time-dependent numerical code (Asano & Mészáros 2011) can follow evolutions of electron energy-distribution and photon production in the shell with increasing radius R . Our numerical code was developed for gamma-ray bursts so that the geometry of the jet is assumed to be a cone with a constant half-opening angle θ_j , while the emission region of blazars has been frequently modeled as a spherical blob or cylindrical flow in precedent studies. Here, we assume a narrow cone with $\theta_j = 1/\Gamma$. Given this opening angle, the transverse scale of the jet R/Γ is comparable to the radial scale in the comoving frame. In this case, the curvature effect of the cone is not so important. This geometry is not extremely different from spherical or cylindrical emission zones.

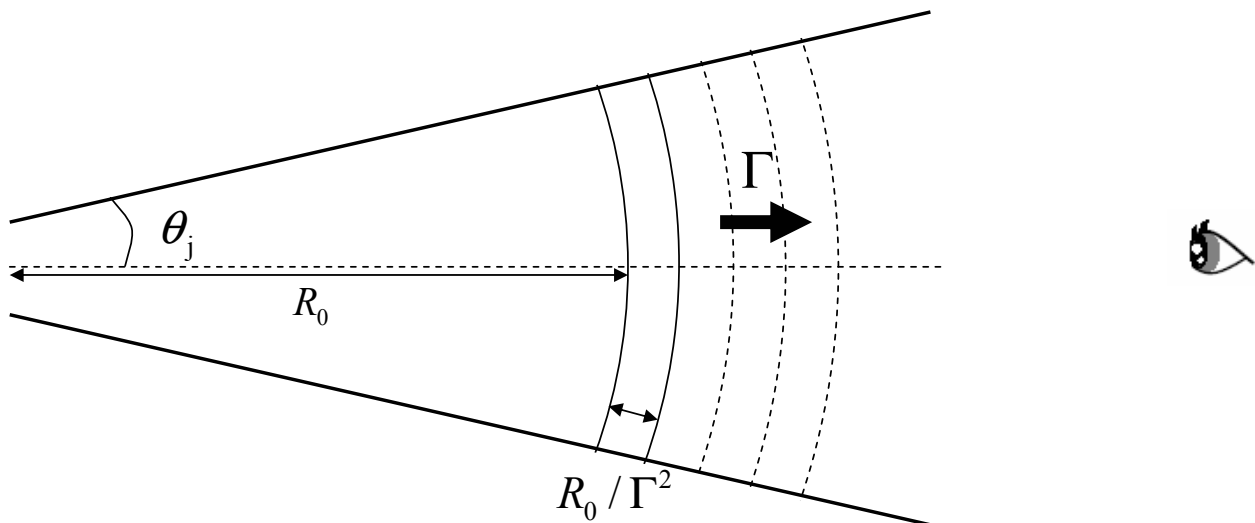


Fig. 1.— Schematic picture of our model.

We regard this thin shell as a homogeneous region, and particle distributions are assumed to be isotropic in the comoving frame (one-zone approximation). Our one-zone numerical code includes the effects of electron cooling and injection to obtain the temporal evolutions of the plasma and photon production. In this paper, we also add the acceleration and energy-diffusion effects by plasma wave turbulences.

The evolution of the electron momentum-distribution is described by the Fokker–Planck

equation as

$$\frac{\partial f_e(p, t)}{\partial t} = \frac{1}{p^2} \frac{\partial}{\partial p} \left[p^2 D_{pp}(p) \frac{\partial f_e(p, t)}{\partial p} + p^2 \langle \dot{p} \rangle_{\text{cool}} f_e(p, t) \right] - \frac{\dot{V}}{V} f_e(p, t) + \dot{f}_{e, \text{inj}}(p, t), \quad (1)$$

where we have assumed an isotropic and homogeneous distribution for the distribution function $f_e(p, t)$. The electrons are assumed to be confined in a volume V . The term with \dot{V}/V expresses the density decrease due to the volume expansion, where \dot{V} is the volume expansion rate. The effects of radiative/adiabatic cooling and particle injection are described using the momentum loss rate $\langle \dot{p} \rangle_{\text{cool}} > 0$, and $\dot{f}_{e, \text{inj}}(p, t)$, respectively. For ultra-relativistic particles, their energies can be approximated as $\varepsilon_e = cp$. The homogeneous approximation allows us to describe the total energy-distribution function as $N_e(\varepsilon_e, t) = 4\pi p^2 c^{-1} f_e(p, t) V$. Then, converting the diffusion coefficient $D_{pp}(p)$ into $D(\varepsilon_e) = c^2 D_{pp}(p)$, eq. (1) becomes

$$\frac{\partial N_e(\varepsilon_e, t)}{\partial t} = \frac{\partial}{\partial \varepsilon_e} \left[D(\varepsilon_e) \frac{\partial N_e(\varepsilon_e, t)}{\partial \varepsilon_e} \right] - \frac{\partial}{\partial \varepsilon_e} \left[\left(\frac{2D(\varepsilon_e)}{\varepsilon_e} - \langle \dot{\varepsilon}_e \rangle_{\text{cool}} \right) N_e(\varepsilon_e, t) \right] + \dot{N}_{e, \text{inj}}(\varepsilon_e, t), \quad (2)$$

where $\langle \dot{\varepsilon}_e \rangle_{\text{cool}}$ is the energy loss rate, and $\dot{N}_{e, \text{inj}}(\varepsilon_e, t)$ is the total electron injection rate. Electrons are gradually accelerated via scattering by turbulences. If the average scattering frequency ν and the fractional energy-change per scattering $\bar{\xi}$ are given, the diffusion coefficient is written as

$$D(\varepsilon_e) = \frac{\bar{\xi}}{2} \varepsilon_e^2 \nu. \quad (3)$$

A collision with a fluid element of velocity $\beta_d \ll 1$ yields $\bar{\xi} \simeq 4\beta_d^2/3$. The average velocity of turbulence may be determined by Alfvén velocity or sound velocity. A fluid with a relativistic temperature (the sonic speed is $c/\sqrt{3}$) gives an extreme limit as $\bar{\xi} \simeq 2/3$. The quasi-linear theory implies that the collision frequency ν is proportional to the gyration frequency $\Omega = eBc/\varepsilon_e$ as

$$\nu \equiv \frac{\pi k |\delta B^2|_k}{4 B^2} \Omega, \quad (4)$$

where $k \simeq eB/\varepsilon_e$ is the wavenumber of turbulence that resonates with the gyration of electrons (Blandford & Eichler 1987). The Fourier transform of the magnetic turbulence is assumed to be a power-law function as $|\delta B^2|_k \propto k^{-q}$. Then, as is well known, the diffusion coefficient becomes a power-law function as

$$D(\varepsilon_e) = \frac{\bar{\xi} \pi e c \varepsilon_e k |\delta B^2|_k}{8B} \equiv K \varepsilon_e^q. \quad (5)$$

As shown in Dung & Schlickeiser (1990), the cross helicity state of the Alfvén waves can affect the momentum diffusion coefficient. However, here we simply extrapolate the above formula for isotropic turbulences in the shell.

In our numerical procedure, for each time-step, after the calculation for electron cooling, the differential terms including $D(\varepsilon_e)$ in eq. (2) are evaluated with the MUSCL scheme with second order accuracy (van Leer 1979) for first-order differentiation, and central-difference method for second-order differentiation. In Figure 2 our test calculations neglecting the electron cooling are shown. Here, we continuously inject electrons of 10^7 eV at a constant rate. The acceleration timescale is roughly written as $t_{\text{acc}} \sim \varepsilon_e^2/2D(\varepsilon_e) \propto \varepsilon_e^{2-q}$. So the steady state solution provides a power-law distribution $N_e(\varepsilon_e) \propto \varepsilon_e^{1-q}$. In Figure 2 we normalize time by the acceleration timescale for 10^{10} eV, $t_0 \equiv (10^{10}\text{eV})^2/(2D(10^{10}\text{eV}))$. The spectral evolutions agree with the acceleration timescale and spectral index estimated above. The cooling effect in this code is also checked. Schlickeiser (1985) provides time-dependent formulae of the electron distribution under the simultaneous action of synchrotron and inverse Compton radiation losses competing with Fermi-I and -II accelerations. Here, we simply demonstrate a steady-state case in Fermi-II models. When the Fermi-II acceleration is balanced with synchrotron energy losses, the electron distribution becomes a Maxwell-like function $N_e(\varepsilon_e) \propto \varepsilon_e^2 \exp\{-(\varepsilon_e/\varepsilon_c)^{3-q}\}$ (Lefa, Rieger & Aharonian 2011), which is identical to the steady state solution of Schlickeiser (1985). The inset figure in Figure 2 shows a quasi-steady distribution after switching off the injection but with acceleration for $q = 2$. In this test calculation, we consider only synchrotron cooling. The distribution agrees with the analytical one (dashed line).

The energy source of the turbulence may be dissipation of the bulk kinetic energy of the jet. In those cases, jets are expected to be decelerated. However, for simplicity, we assume a constant Lorentz factor Γ throughout this paper. If internal fluid-motions exist in the jet at $R < R_0$, the dissipation of the internal motions can be the energy source. This model may validate the constant Lorentz factor in our simulations. Anyway we do not specify the dissipation source for the turbulences, and the second order Fermi acceleration is phenomenologically treated with the parameter K .

Hereafter, we will fix the index q in eq. (5) at the Kolmogorov value $5/3$ for simplicity. The diffusion coefficient should be determined by the characteristics of turbulences. At present we have no definite theory for magnetic turbulences in blazar jets. To reproduce observed spectra, we will adjust diffusion coefficients below. If the coefficient K in eq. (5) is larger than a value $K_{\text{max}} \sim (\gamma_{\text{max}} m_e c^2)^{1/3} \Omega$ estimated from eq. (4) with an extreme limit $\bar{\xi} k |\delta B^2|_k / B^2 \sim 1$ at $\varepsilon_e \sim \gamma_{\text{max}} m_e c^2$, it is physically unrealistic. As will be seen below, the values of K we adopt are safely smaller than $K_{\text{max}} \sim (\gamma_{\text{max}} m_e c^2)^{-2/3} e B c \simeq 1.4 \times 10^4 (B/0.1 \text{ G})(\gamma_{\text{max}}/10^6)^{-2/3} \text{ eV}^{1/3} \text{ s}^{-1}$.

For simplicity, the electron injection is assumed to be mono-energetic; the electron Lorentz factor at injection will be fixed as $\gamma'_{\text{inj}} = 100$. Hereafter, the quantities in the

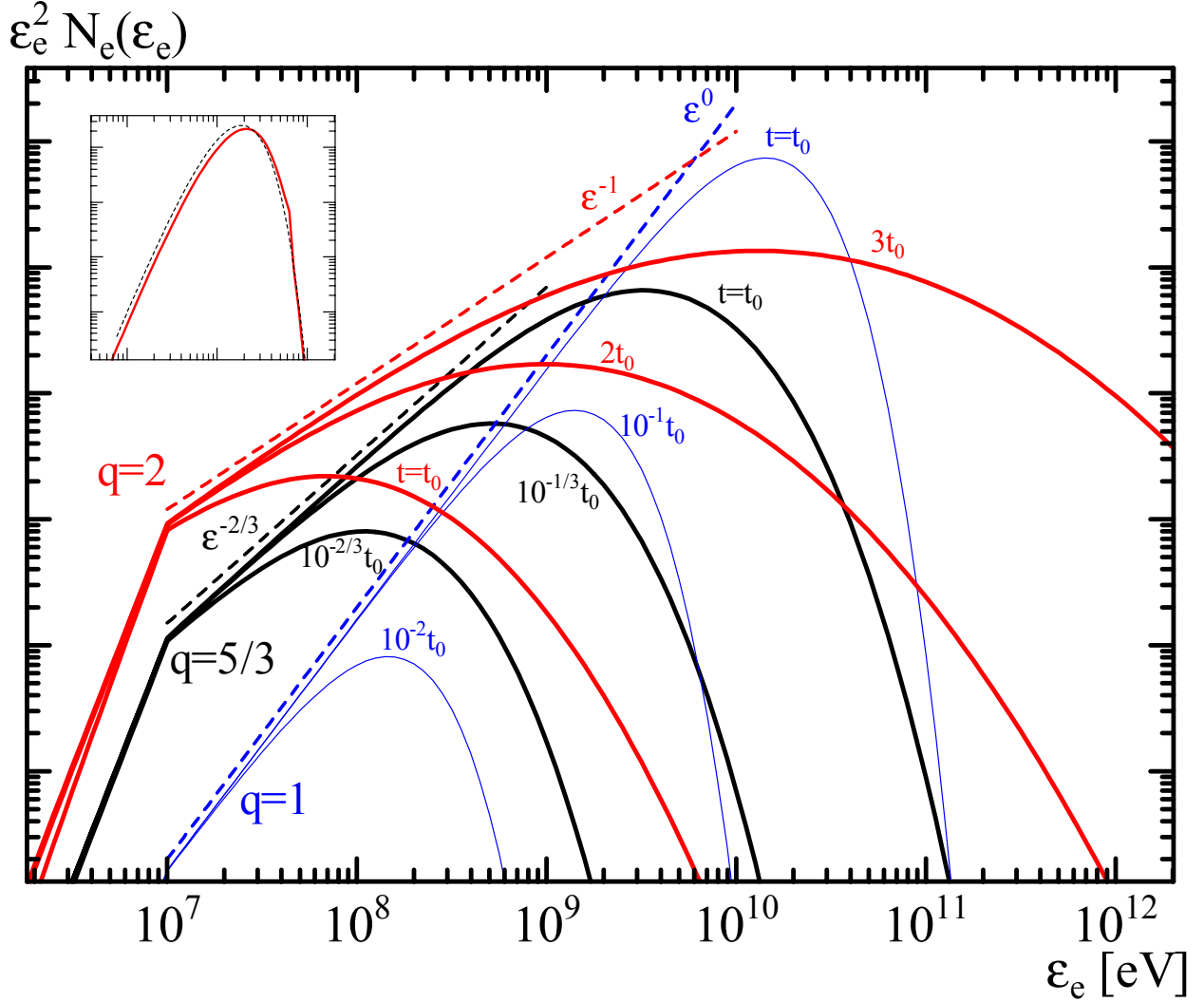


Fig. 2.— Test calculations for the evolution of the electron energy distribution with the Fermi-II acceleration for various indices q . Here, we neglect the radiative cooling and volume expansion. The labels for the dashed lines show a power-law form for the energy distribution $N_e(\varepsilon_e)$, while the vertical axis (in arbitrary units) is $\varepsilon_e^2 N_e(\varepsilon_e)$. The inset figure shows a quasi-steady spectrum due to the balance between the acceleration and synchrotron cooling (arbitrary units). This agrees with the Maxwell-like function (dashed line).

comoving frame are denoted with primed characters. As the shell outflows, the injected electrons are gradually accelerated following eq. (2). As the emission region flows outward, the volume increases as $V' \propto R^2$ in this conical geometry. The adiabatic cooling is taken into account with the same method as Asano & Mészáros (2011), in which the electron energy decreases as $\varepsilon'_e \propto V'^{-1/3}$ in the ultra-relativistic limit. The electrons remaining in the shell

cool adiabatically, and the emission will cease as the shell expands even if electrons do not escape from the shell.

We do not include the effect of the electron escape in this paper as shown in eq. (1). This is a critical process to obtain the electron spectrum as is well known. In our quasi-steady outflow model depicted in Fig. 1, the electron escape is equivalent to the electron transfer between shells. Our one-zone approximation is not optimized for the electron transfer. However, the isotropic diffusion we assumed may allow us to neglect the escape, because the escape rate from a shell may be almost equal to the incoming rate from adjoining shells. Given the mean free path $l_m = c/\nu$, the spatial diffusion coefficient can be approximated as $D_{xx} = l_m c/3$. Then, the diffusion length in the dynamical timescale W'/c becomes $\langle \delta x' \rangle = \sqrt{D_{xx} W'/c}$, which implies

$$\frac{\langle \delta x' \rangle}{W'} = \sqrt{\frac{\bar{\xi} \bar{\xi}_e^{1/3} c}{6W'K'_0}} \simeq 0.7 \bar{\xi}^{1/2} \left(\frac{W'}{10^{16} \text{ cm}} \right)^{-1/2} \left(\frac{K'_0}{10^{-2} \text{ eV}^{1/3} \text{ s}^{-1}} \right)^{-1/2} \left(\frac{\bar{\xi}_e}{10^{12} \text{ eV}} \right)^{1/6}, \quad (6)$$

for $q = 5/3$. For a conservative value of $\bar{\xi} \ll 1$, the spatial diffusion is not so sufficient. This also supports the neglect of the escape effect in our model.

The average magnetic field should decay with radius, unless some kind of amplification mechanism works. In this paper we assume a power-law evolution as $B' = B_0(R/R_0)^{-1}$, which implies conservation of magnetic energy.

In each time step, photons are produced in the shell with a rate that is consistent with the electron cooling rate. The photon production processes we adopt are synchrotron and inverse Compton (IC) emissions. The Klein-Nishina effect on IC emission is fully included in our numerical method. The photon density is evaluated with the homogeneous approximation taking into account the photon escape from the shell (see Asano & Mészáros 2011, for details). We adopt this spectral density of photons to estimate the seed photons for IC scattering. Our one-zone approximation does not solve the radiative transfer in the steady outflow. Therefore, the escaped photons are not counted as the seed photons for IC scattering. Such photons may contribute to the seed photons in regions outside the original shell. However, we take into account only the photons remaining in the shell. This problem in our method may be absorbed by the uncertainty in the model setting (simplified geometry, electron injection etc.). The photon absorption via $\gamma\gamma$ collision, secondary electron-positron pair injection, and synchrotron self-absorption are also included in our code. But, those effects are not so important in our examples below.

The evolution of accelerated particles and photon production in a shell are computed with the time-dependent method as we explained. Considering the curvature effect, Doppler boost due to the relativistic bulk motion of the shell, and the opening angle θ_j , we can

estimate the arrival time and energy of photons escaping from the shell for an observer. Based on those outputs, the temporal evolution of the photon spectrum emitted from “one shell” can be obtained. High energy photons can be absorbed via $\gamma\gamma$ collision with EBL during the propagation in the intergalactic medium. To obtain spectra for observers, we adopt the model in Kneiske et al. (2004) for EBL evolution.

The central engine may continuously eject shells that emit photons. Photons escaping from different shells can arrive at an observer simultaneously. We can model temporal evolutions of blazar emissions by accumulating the contributions of such shells with different launch times. If we change the model parameters for each shell, various models including a steady emission will be realized. To model a steady emission from a steady flow, we assume that identical shells are continuously ejected at $R = R_0$ with a time step of $R_0/(c\beta\Gamma^2)$. The steady spectrum for an observer is comprised of the contributions of all shells at $R \geq R_0$. The time-integrated spectrum from one shell provides the average spectral shape from the steady flow. The steady spectral flux is easily obtained by dividing the time-integrated spectrum emitted from one shell with the shell ejection time step $R_0/(c\beta\Gamma^2)$.

For the steady emission model, the model parameters are six: the initial radius R_0 , radius where the injection and acceleration cease R_c , bulk Lorentz factor Γ , initial magnetic field B_0 , injection rate \dot{N}'_e , and diffusion coefficient K' . They are minimum parameters required in our model. In §4, we will additionally consider the radial evolutions of \dot{N}'_e and K' . In this case, the power-law indices are introduced as two additional parameters. The number of parameters are not so many compared to the precedent models. For example, the model parameters for Mrk 421 in Abdo et al. (2011), one-zone synchrotron self-Compton (SSC) model, are 11.

3. 1ES 1101-232

First we adopt the Fermi-II acceleration model to TeV blazar 1ES 1101-232 (Aharonian et al. 2007a). The detection of TeV gamma-rays from this high redshift ($z = 0.186$) object aroused interest in view of the constraint on EBL (Aharonian et al. 2006). The *Fermi* telescope provided a stringent upper limit in GeV energy range (Neronov & Vovk 2010). This implies a very hard spectrum from GeV to TeV.

The model parameters for this blazar are $\Gamma = 25$, $B_0 = 0.03$ G, and $W' = R_0/\Gamma = 2.8 \times 10^{16}$ cm. We inject electrons with a constant rate $\dot{N}'_e = \dot{N}_0 = 1.5 \times 10^{46} \text{ s}^{-1}$ in spherically symmetric evaluation during a timescale of $\Delta T'_{\text{inj}} = W'/c$ in the shell frame. This implies that the electron injection ceases at $R = 2R_0$. In this injection timescale, a turbulence in

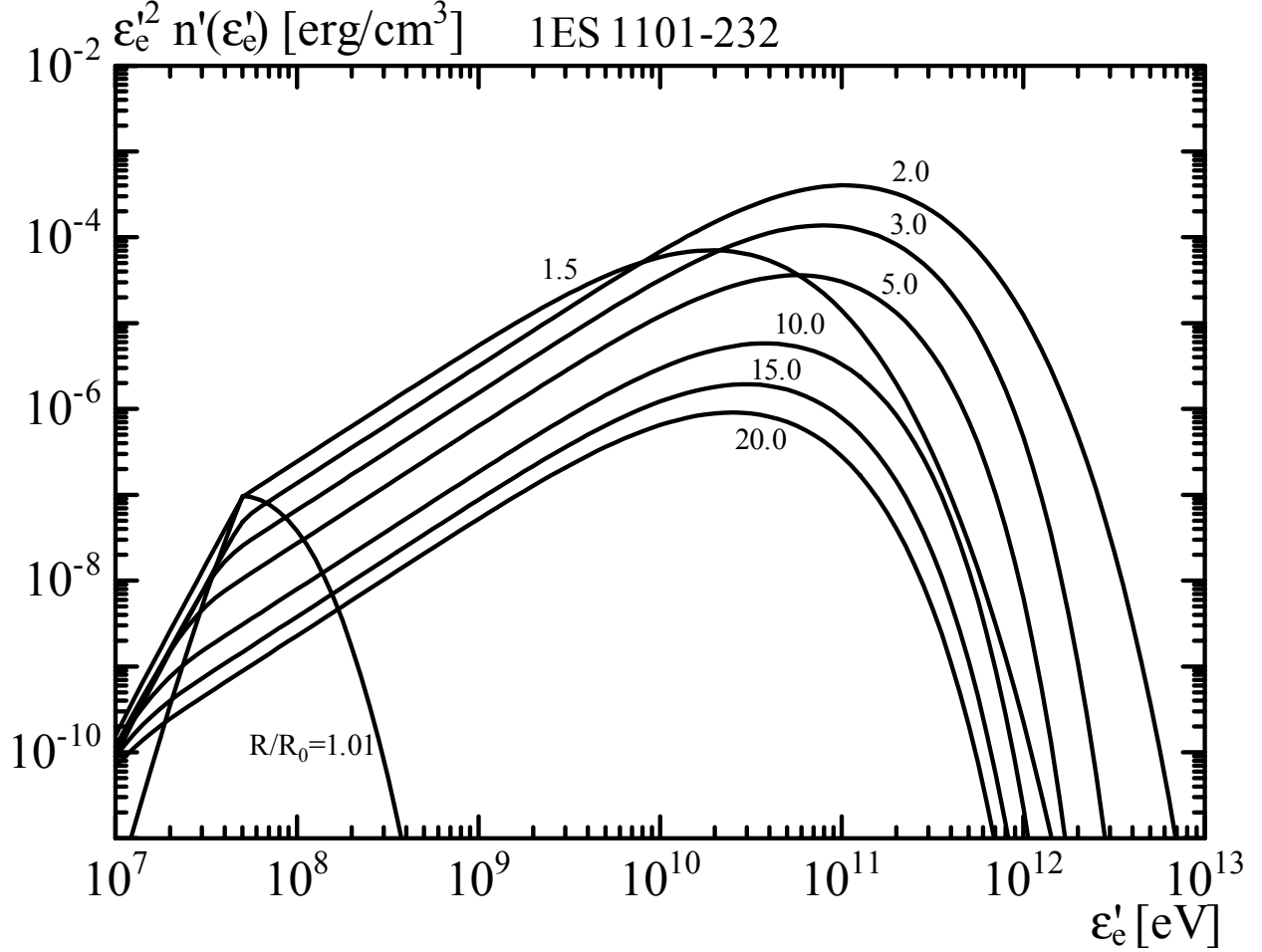


Fig. 3.— Evolution of the electron energy distribution for 1ES 1101-232

the shell accelerates electrons with the diffusion coefficient $K' = 4.3 \times 10^{-3} \text{ eV}^{1/3} \text{ s}^{-1}$. After the end of the electron injection, we assume that the turbulence is terminated as well, so electrons cool monotonically via radiation and adiabatic expansion.

Figure 3 shows the evolution of the electron energy distribution in the shell frame. As the electron injection and acceleration proceed, the electron energy density grows and achieve a maximum at $R = 2R_0$. The $\epsilon_e'^2 n'(\epsilon_e')$ -spectrum has a maximum at $\sim 10^{11}$ eV, where $n'(\epsilon_e') \equiv N'_e(\epsilon_e')/V'$. This peak energy is determined by the duration time of the acceleration, which corresponds to the acceleration timescale of this energy. After the end of the electron injection and acceleration, the shell expansion causes the density drop, and adiabatic cooling lowers the electron energy. Thus, the spectral peak energy shifts to lower energies as the shell expands. The effect of the radiative cooling is seen as the growth of the sharpness of the spectral cut-off above the peak energy.

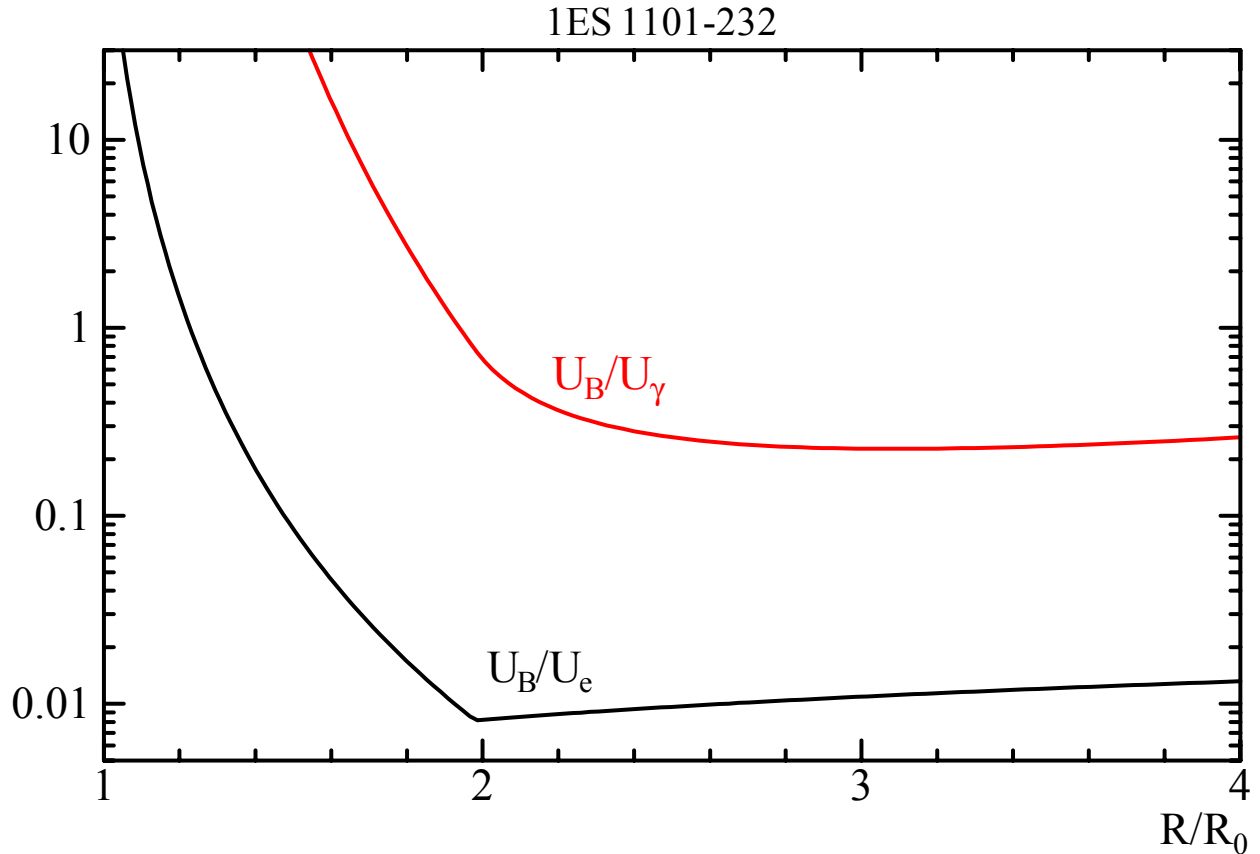


Fig. 4.— Evolution of the energy density ratios in a shell in the model for 1ES 1101-232. The energy densities of photons, electrons, and magnetic fields in the shell frame are denoted as U_γ , U_e , and U_B , respectively.

In this parameter set, the radiative cooling is not so efficient that the photon energy density is always lower than the electron energy density, as indirectly shown in Figure 4. Nonetheless, the photon energy density overtakes the magnetic energy density in the later phase, which leads to sufficient SSC emission.

The steady state spectrum obtained from our model is shown in Figure 5. Our simple assumption (constant injection and diffusion coefficient) succeeds in reproducing the observed hard spectrum avoiding the *Fermi* upper limit. The hard electron spectrum due to the Fermi-II acceleration naturally leads to this hard spectrum.

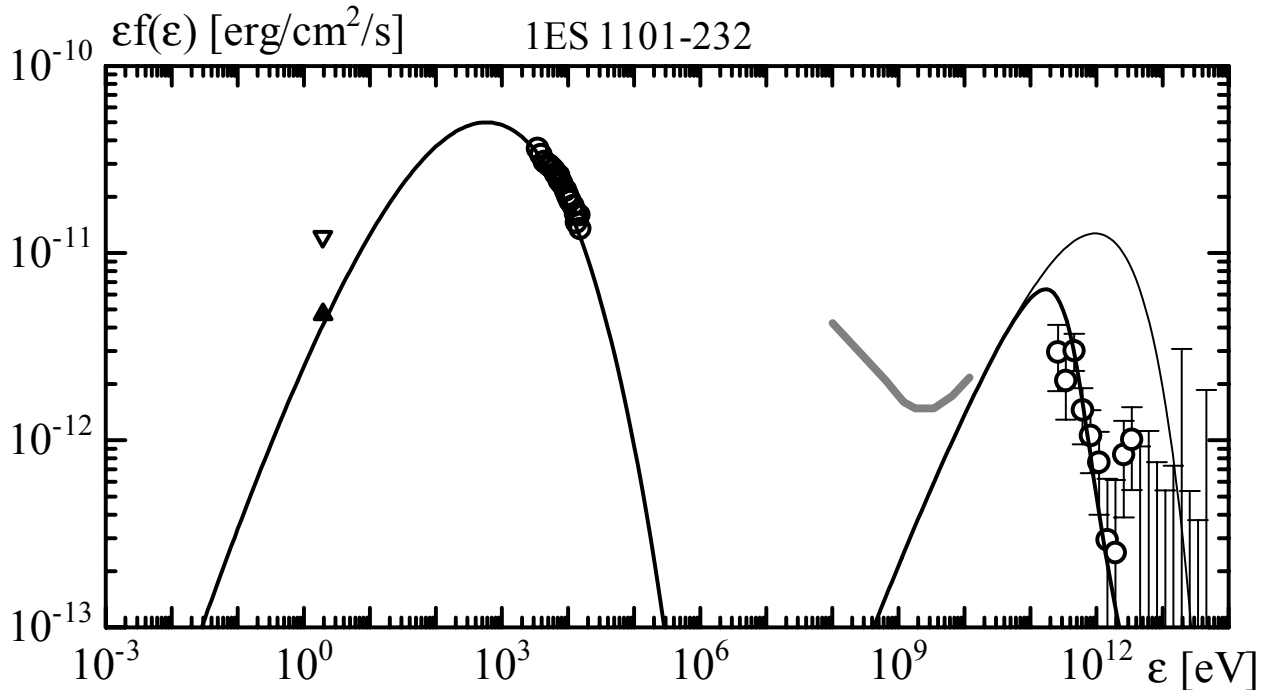


Fig. 5.— Steady photon spectrum for 1ES 1101-232. The data points are from Aharonian et al. (2007a), and the *Fermi* upper limit in Neronov & Vovk (2010) is also shown with the bold grey line. The thin line for the IC component is the spectrum without the absorption effect due to EBL.

4. Steady Emission in Mrk 421

The Fermi-II acceleration model can naturally explain the hard-spectrum blazar as shown in the previous section. If this acceleration mechanism is universal in the quasi-steady emissions from blazars, relatively softer spectra for other ordinary blazars should be also fitted by this model. However, the hard spectra obtained from the simplest model apparently contradict the observed one. In order to overcome this problem, we consider the temporal (equivalently radial) evolutions of the electron injection rate and diffusion coefficient.

As a representative example of blazars, we consider Mrk 421 at $z = 0.031$, whose wide-band spectrum from radio to TeV is one of the most precisely observed spectra. Here we adopt the spectrum obtained from the 4.5 month long multifrequency campaign (2009 January 19 to 2009 June 1, Abdo et al. 2011). During this campaign, Mrk 421 showed low activity and relatively small flux variations at all frequencies. Thus, this data set is well qualified to study steady emissions from blazars. In Abdo et al. (2011), to fit the obtained

spectrum by leptonic models, an electron distribution of three power-law functions (namely two breaks) is required. This may be because the spectral shape around the peak energy from optical to X-ray bands is too broad for single break models. While the origin of such spectral breaks is unknown, the time-dependent model may provide us a new possible picture for this blazar.

For electrons injected at a later phase, the effective duration of the acceleration becomes shorter than that of electrons injected initially. Such later-injected electrons remain in the low-energy region. Therefore, an increase of the injection rate for a finite injection timescale leads to a softer electron spectrum than that with a constant injection rate. The diffusion coefficient may also evolve with time. A decrease of the diffusion coefficient makes later-injected electrons remain in low-energy. However, a too rapid decline of K' results in a too low maximum energy of electrons. In order to reproduce the observed spectrum, hereafter, we adjust the evolution of \dot{N}'_e , while the evolution of K' is fixed as $K' \propto R^{-1}$ for simplicity.

4.1. Simple SSC model

Figure 6 shows the result obtained from our model with the temporal evolutions of the injection rate and diffusion coefficient. The model parameters are $\Gamma = 15$, $B_0 = 0.13$ G, and $W' = R_0/\Gamma = 1.0 \times 10^{16}$ cm. The duration time of the electron injection and acceleration is assumed to be $\Delta T'_{\text{inj}} = 2W'/c$ (end at $R = 3R_0$), which is taken longer than the assumption in 1ES 1101-232 to enhance the effects of the temporal evolutions. In this duration time, the injection rate is assumed to evolve as $\dot{N}'_e = \dot{N}'_0(R/R_0)^7$, where $\dot{N}'_0 = 9.8 \times 10^{43} \text{ s}^{-1}$. Similarly, the diffusion coefficient evolves as $K' = K_0(R/R_0)^{-1}$, where $K_0 = 1.3 \times 10^{-2} \text{ eV}^{1/3} \text{ s}^{-1}$.

The synchrotron component is well reproduced by this model. An advantage of this model is that the curved spectral feature is naturally explained by the power-law evolutions of injection and diffusion, while the usual shock acceleration models need breaks at ad hoc energies in the injection spectrum.

The curved photon spectrum is a direct consequence of the curved electron spectrum as shown in Figure 7. The electron spectra are softer than the case in 1ES 1101-232 owing to the temporal evolution of the electron injection. Just above $\varepsilon'_e = \gamma'_{\text{inj}} m_e c^2$, the electron spectral index is about 1.06, but the spectrum gradually becomes softer with energy. After the acceleration ceases, the electron spectra show a sharper cut-off due to the radiative cooling (see thin lines). For reference, we also plot the analytic model spectra in Abdo et al. (2011) and Tramacere et al. (2009). The double broken power-law (DBP) model in Abdo et al. (2011) has breaks at 2.6×10^{10} eV and 2.0×10^{11} eV with indices of 2.2, 2.7, and 4.7 from

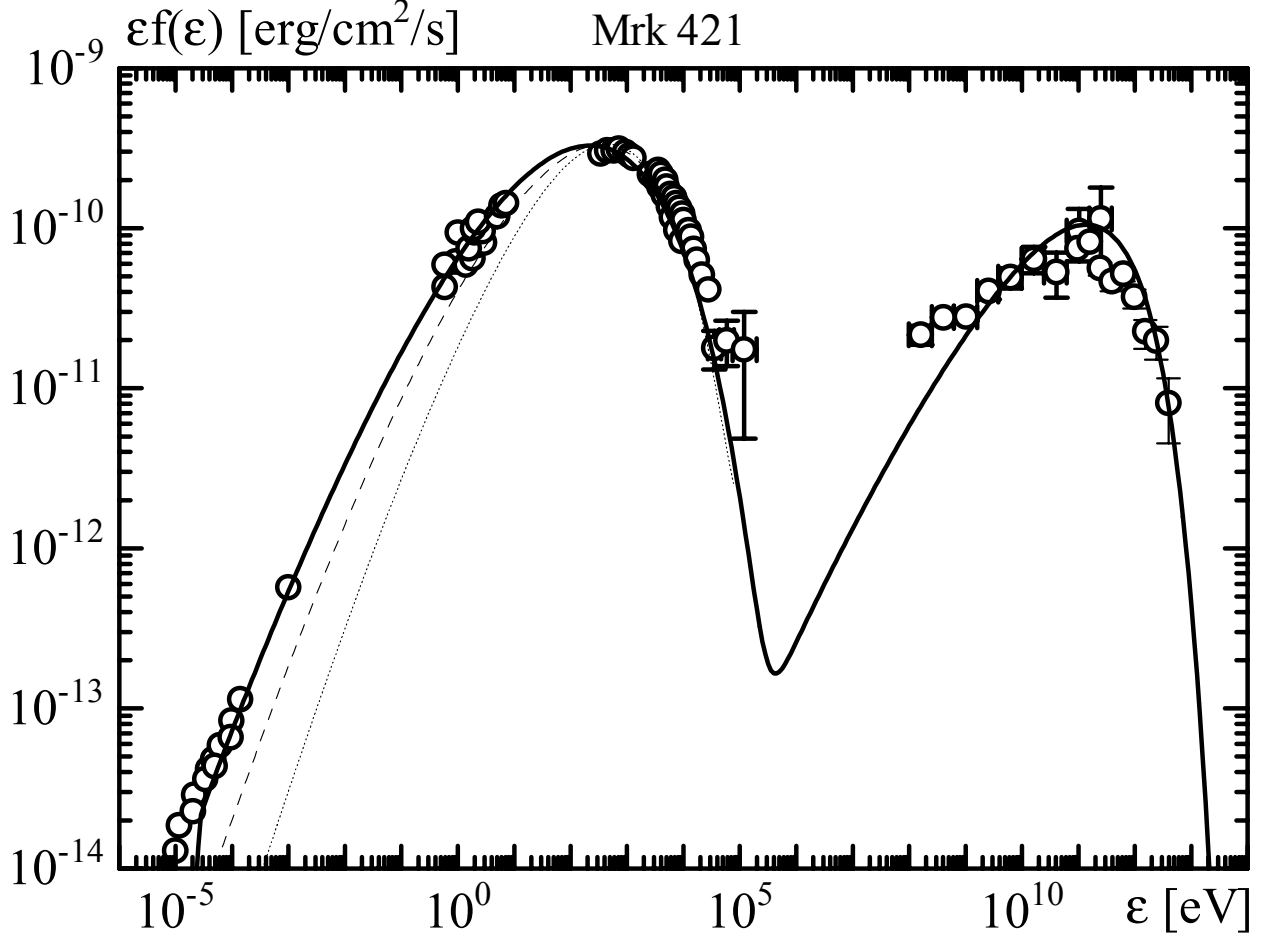


Fig. 6.— Steady photon spectrum for the simple SSC model of Mrk 421 (see §4.1). The data points are partially extracted from the data of the 4.5 month campaign (Abdo et al. 2011). For reference, synchrotron spectra with different parameter evolutions, $\dot{N}'_e \propto R^7$ and $K' \propto R^0$ (thin dashed line), and $\dot{N}'_e \propto R^0$ and $K' \propto R^{-1}$ (thin dotted line), are plotted.

low to high energy portions. The model in Tramacere et al. (2009) is a combination of a power-law at low energies (index 2.3) and a log-parabolic high-energy branch,

$$n'(\epsilon'_e) \propto \epsilon'^{-2.3-0.75 \ln(\epsilon'_e/\epsilon_j)}, \quad (7)$$

where the joint of the two functions is at $\epsilon_j = 8.9 \times 10^{10}$ eV. Note that this log-parabolic model was adopted to fit the spectral data of 22-04-2006, while the DBP model is for the same data set with ours. Those two analytic models have similar shapes to ours between 10^{10} eV and 10^{12} eV so that all the models can fit the synchrotron component around the peak.

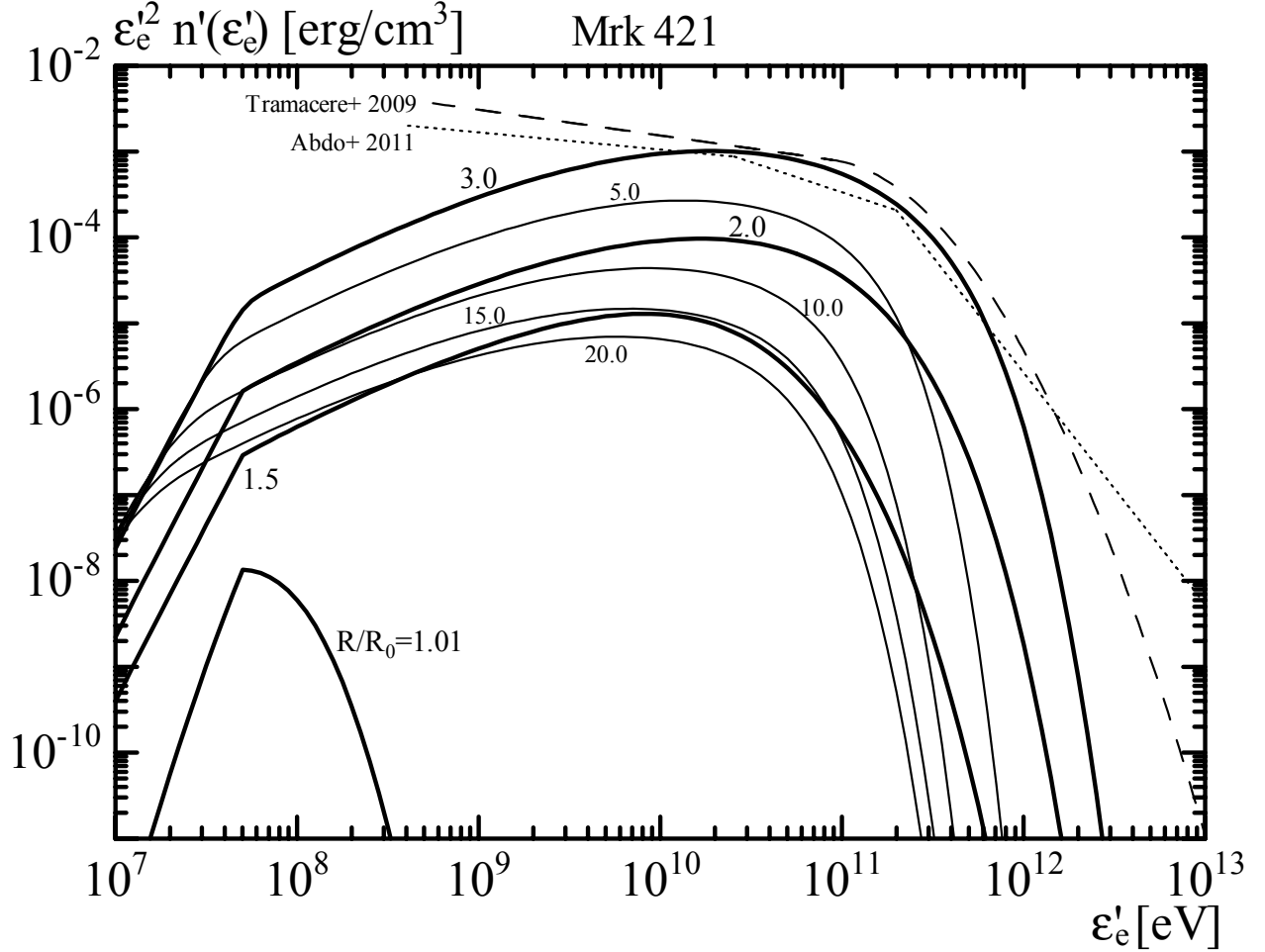


Fig. 7.— Evolution of the electron energy distribution for the model of Mrk 421 in Fig. 6. The electron spectra during the acceleration process are denoted by thick lines, while those after the end of the acceleration are denoted by thin lines. The spectral shapes of other one-zone leptonic models are plotted (in arbitrary units) for reference. The thin dotted line is the double broken power-law model in Abdo et al. (2011), and the thin dashed line is the log-parabolic model in Tramacere et al. (2009).

In the two models with analytic functions, the soft spectra below $\sim 10^{10}$ eV are advantageous to fit the GeV spectrum, while our model flux is significantly lower than the flux data obtained with *Fermi*. It may be hard to make such a soft spectrum in this energy range in Fermi-II models. However, the power-laws for the two analytic models below 10^9 eV are too soft to reconcile with the radio spectrum. Hence, the analytic models require another break or low-energy cut-off below 10^9 eV. To discriminate these distributions, future infrared and submillimeter observations are interesting.

The hard electron spectrum in our model yields the radio emission that agrees with the observed spectrum. In most of preceding models based on shock acceleration, abundant low energy electrons for an power law index of 1.5-2.0 make the synchrotron self absorption frequency at a submillimeter range. Hence, another component, such as synchrotron self-absorbed emissions from inhomogeneous jet (e.g. Königl 1981) etc., has been required to reconcile the radio observations. In contrast, the electron spectrum at low energy part is rather hard with a power law index approximately 1.06 even though we increased low energy particles with an evolution of injection. So that synchrotron self-absorption is negligible in our model.

Let us confirm this statement analytically. At $R = 3R_0$, the spectral density is $n'(\varepsilon'_e) \simeq 2200 \text{ erg}^{-1} \text{ cm}^{-3}$ at $\varepsilon'_e = \gamma'_{\text{inj}} m_e c^2$. If we denote this as $n'(\varepsilon'_e) = C\varepsilon'^{-1}_e$, $C \simeq 0.18 \text{ cm}^{-3}$, which is comparable to the density $\sim 1 \text{ cm}^{-3}$ obtained with the time-integrated number of electrons, $3^8 R_0 \dot{N}_0 / 8c\Gamma$ (note $dt'/dR \simeq 1/c\Gamma$), and volume, $V' = 4\pi(3R_0)^2 W'$. The formula in Rybicki and Lightman (1979) gives us the optical depth due to synchrotron self-absorption as

$$\tau_{\text{SSA}} = 1.3 \times 10^{-2} \left(\frac{C}{0.18 \text{ cm}^{-3}} \right) \left(\frac{B'}{0.1 \text{ G}} \right)^{3/2} \left(\frac{\varepsilon'}{10^{-5} \text{ eV}} \right)^{-5/2} \left(\frac{W'}{10^{16} \text{ cm}} \right), \quad (8)$$

or the break photon energy, defined as $\tau_{\text{SSA}}(\varepsilon'_a) = 1$, becomes

$$\varepsilon'_a = 1.8 \times 10^{-6} \left(\frac{C}{0.18 \text{ cm}^{-3}} \right)^{2/5} \left(\frac{B'}{0.1 \text{ G}} \right)^{3/5} \left(\frac{W'}{10^{16} \text{ cm}} \right)^{2/5} \text{ eV}. \quad (9)$$

As shown in Figure 7, the low-energy electron density in our model is much less than the extrapolations of the analytic models. As we have mentioned, this is one of reasons why the self-absorption frequency is relatively low. Differently from the assumption in the above analytical estimate of eq. (9), the electron distribution has a break at $\gamma_e = \gamma_{e,\text{inj}} = 100$, so that the above break energy would lower. Thus, the spectral break at $\varepsilon \sim 10^{-5} \text{ eV}$ is mainly due to the break in the electron spectrum rather than the absorption effect. The actual $\gamma_{e,\text{inj}}$ may be less than that we assumed ($\gamma_{e,\text{inj}}$ has been set as 100 to save computational cost). So the electron spectrum in our model can comprehensively explain the spectrum from radio to X-ray without introduction of the minimum Lorentz factor $\gamma_{e,\text{min}}$.

In our model, while the diffusion coefficient decreases, the sharp rise of the injection rate ($\dot{N}'_e \propto R^7$) is required, which may seem unnatural. The electron injection rate is determined by short wavelength turbulences that resonate with the gyro motion of low-energy electrons. Such waves may have different evolution from the turbulences that accelerate high-energy electrons. While the long waves are produced by large-scale instability, such as the Kelvin-Helmholtz instability etc., the origin of the short waves may be the cascade of the long

waves. In this case, the efficiency of the electron injection may grow later relatively to the development of the long waves. Another possibility is the evolution of the low-energy threshold to be accelerated. Let us consider electrons at energies of the cut-off tail in the Maxwellian distribution. When the minimum wavelength is relatively long, only higher energy electrons can be injected to the acceleration process. If the minimum wavelength gradually shortens as the cascade proceeds, lower energy electrons are also injected. This mechanism may cause a sharp rise of the injection rate retracing the cut-off shape in the Maxwellian distribution.

We have assumed the evolutions of $\dot{N}'_e \propto R^7$ and $K' \propto R^{-1}$. If either \dot{N}'_e or K' is constant, as shown in Figure 6, the synchrotron spectrum becomes narrower than the observations. The broad peak represented by the X-ray and IR-optical data points is achieved by the combination of those evolutions. Of course, our example of the parameter evolutions may not be a unique solution. On the other hand, we find that the X-ray spectrum shape can be solely fitted without those evolutions, if we neglect IR-optical and radio data. The X-ray spectral shape is determined by the high-energy cut-off shape of the electron spectrum, which may be controlled by the diffusion process in the momentum space and radiative cooling rather than the parameter evolutions.

Our parameter choice reproduces the flux level of the IC component as well. However, the observed flux at ~ 100 MeV is significantly higher than the model spectrum. The spectrum obtained with *Fermi* is relatively flat compared with the synchrotron spectrum. The steady SSC spectrum obtained with our time-dependent model is hard to reconcile with the *Fermi* data.

4.2. SSC+EIC model

The simplest method to fit the GeV flux is an introduction of another emission region that contributes to this energy range. Such two-zone models have been discussed by several authors such as Ghisellini et al. (2005).

Here, we consider another possibility, the effect of an external photon field, to reproduce the 100 MeV–GeV flux in Mrk 421. While external photons are indispensable to explain IC components of flat spectrum radio quasars (FSRQs), BL Lac objects have been fitted without external photons. For FSRQs, optical photons from broad line regions are a candidate for the external photon field. However, the average electron energy in BL Lac objects is much higher than that in FSRQs so that the Klein-Nishina effect makes the contribution of the external optical photons negligible. Moreover, the typical energy range of the IC-scattered optical

photons becomes much higher than the GeV energy range. Here, we consider an external radio photons, which may come from compact radio lobes as seen in young radio-loud AGNs (Snellen et al. 2004).

We consider an external photon field, whose spectral peak in $\varepsilon f(\varepsilon)$ -diagram is 10^{-6} eV (240 MHz). This corresponds to $\sim 10^{-6}\Gamma$ eV $\sim 10^{-5}$ eV in the shell frame, which is safely high enough to avoid synchrotron self-absorption [see eq. (9)]. Since we have no definite model for the spectrum, the Band function (Band et al. 1993), smoothly-joined power-laws, is adopted here. The low- and high-energy photon indices (defined as $-d \ln f(\varepsilon)/d \ln \varepsilon + 1$) are chosen as -1 and 2.5 , respectively. The total luminosity is $L_{\text{ex}} = 4.9 \times 10^{38}$ erg s $^{-1}$. When photons are isotropically distributed, the photon energy density in the comoving frame of the jet is $4U_{\text{ex}}\Gamma^2/3$ (Dermer & Schlickeiser 2002). However, the isotropic approximation may not be accurate. So we neglect the numerical coefficient, and assume the comoving energy density as

$$U'_{\text{ex}} = \Gamma^2 \frac{L_{\text{ex}}}{\pi R^2 c}. \quad (10)$$

The spectral shape is simply shifted by a factor of Γ in the shell frame. Based on this photon distribution in the shell frame, we calculate the contribution of external IC (EIC). Of course, our time-dependent code can wholly take into account the non-linearities of the cooling processes (Zacharias & Schlickeiser 2012). For simplicity, we assume isotropic emissions in the shell frame, though the external photons may be beamed in this frame. Therefore, the contribution of the external photons is simply taken into account by adding the boosted external photons to the photon field in the shell frame. The external component is intrinsically indistinguishable from the internal synchrotron/IC photons.

As shown in Figure 8, the photon energy density is initially dominated by the external photons so that the ratio U_B/U_γ is almost constant. As the electron injection proceeds, photons produced in the shell becomes predominant as seen at $R > 2R_0$, and its energy density overtakes the magnetic one. Similarly to 1ES 1101-232, the emission efficiency is so low that most of the electron energy is not released as radiation.

The final results for our model with external photons are shown in Figure 9, where the model spectrum well agrees with observed spectra from radio to TeV. As we have explained in §2, the steady spectrum is a superposition of emissions from multiple shells at different R . However, the steady photon spectrum is virtually determined by the electron spectral shape at $R = 3R_0$, because the rapid increase of the electron injection makes the electron density become maximum at the end point of the injection/acceleration (see Figure 7). But the emission spectrum from one shell for an observer evolves as shown in Figure 9. The synchrotron component shows a hard-to-soft evolution. This may be due to the decay of the

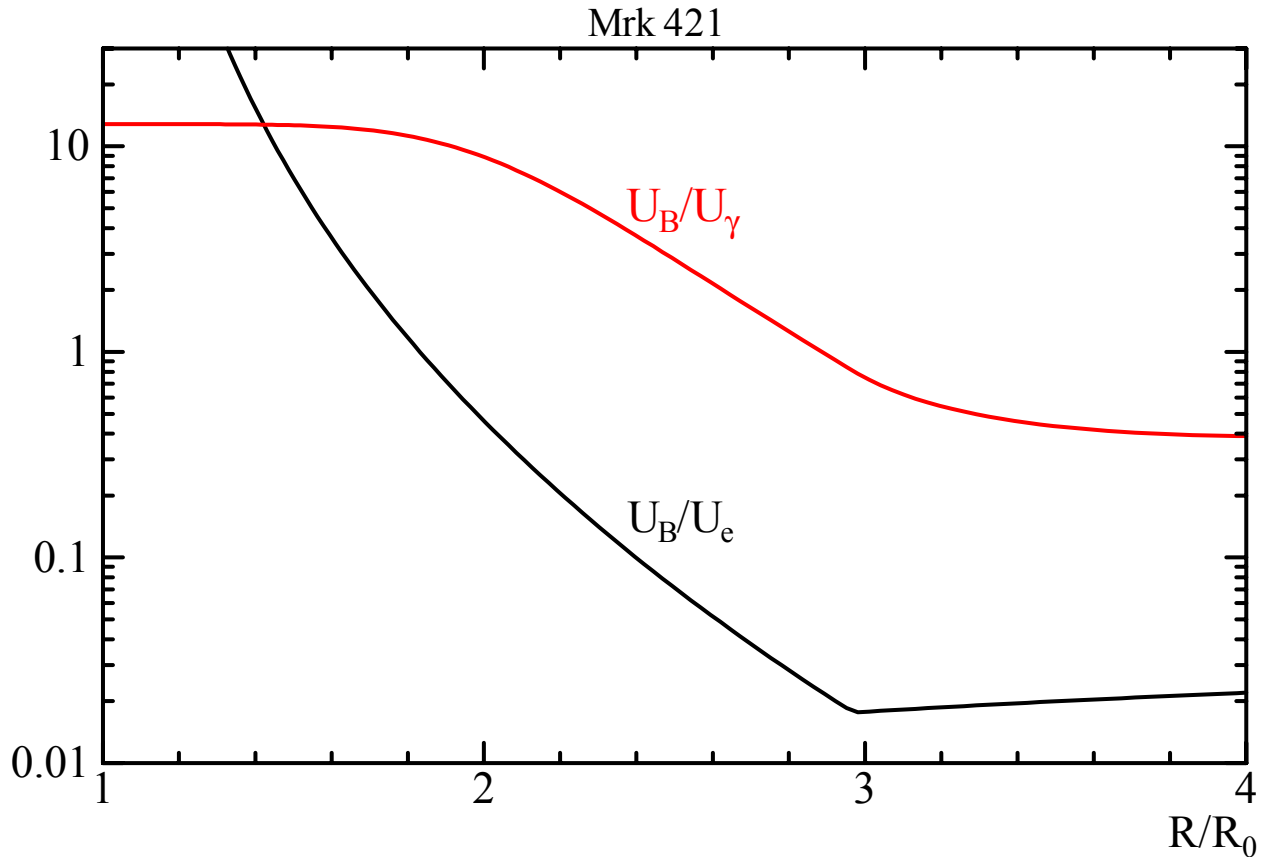


Fig. 8.— Evolution of the energy density ratios in a shell in the model for Mrk 421 with external photons (see §4.2). The label notations are the same as in Fig. 4.

magnetic field. On the other hand, the SSC component, which has a peak around 10^{11} eV, do not show a drastic evolution in its hardness. The Klein-Nishina effect makes a peak at the energy that is determined by the maximum energy of electrons. As a result, this peak energy is insensitive to the synchrotron peak energy. The EIC emission, whose spectral peak is clearly seen in the single-shell spectra especially for the early period (10–32ks), succeeds in reproducing the *Fermi* data.

While two-zone models are still promising, the success of the EIC model encourages single emission-region models. The EIC model needs another parameter set for the external photon field. The essential parameters are its luminosity and peak photon energy, because the details of the photon spectral shape is not so important. Thus, the practical number of the model parameters is 10 in this model (see the last part in §2). This number is still fewer than the DBP model in Abdo et al. (2011), though the DBP model is not designed to address the radio spectrum.

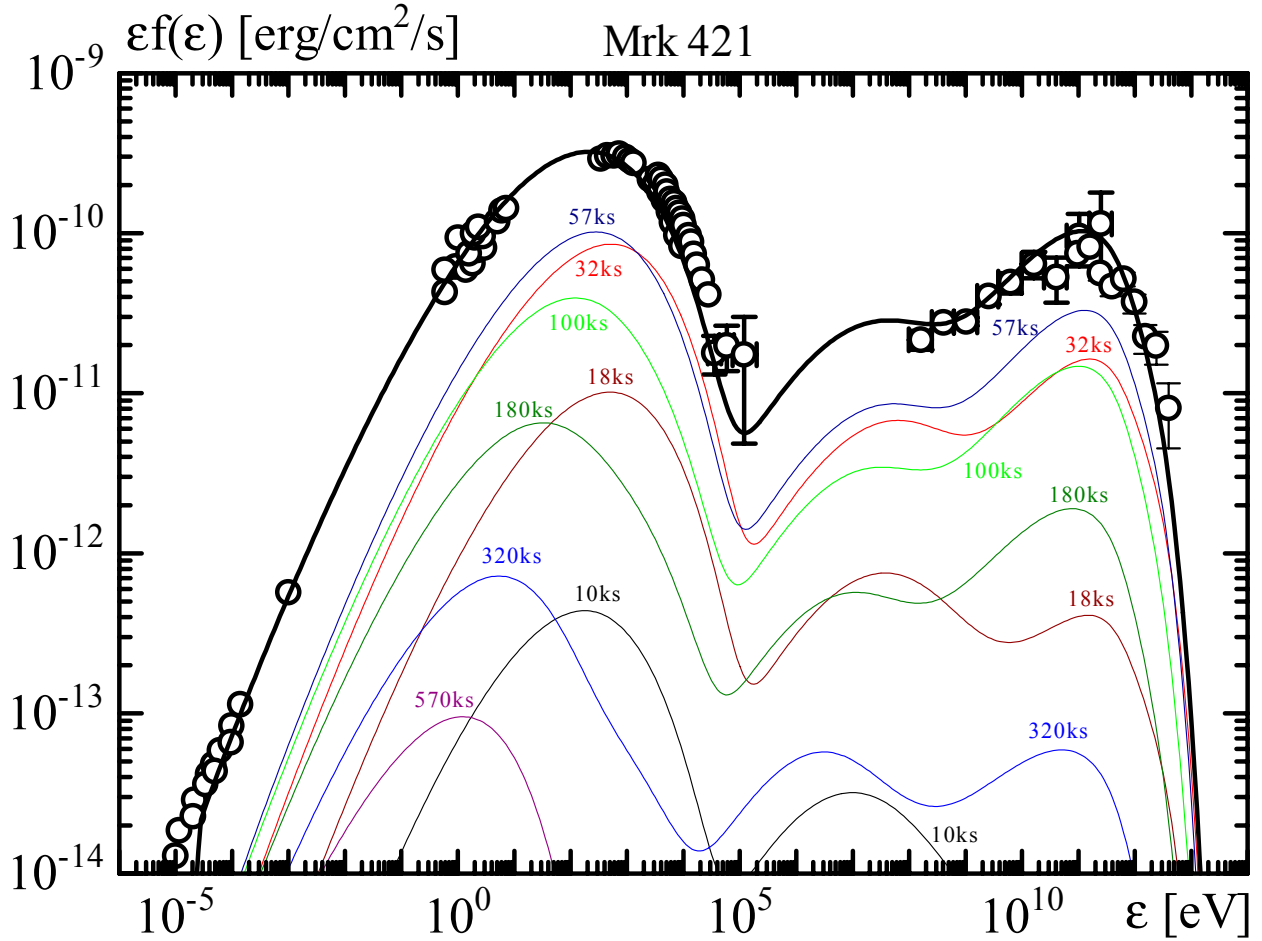


Fig. 9.— Steady photon spectrum (thick) for the model of Mrk 421 with external photons (see §4.2). Thin lines show the evolution of the photon spectrum emitted from one shell, neglecting the emissions from the other shells. The steady spectrum can be interpreted as a superposition of those spectra. The time (ks) labeling each thin line is for observers at earth.

5. Variability in Mrk 421

The MAGIC telescope reported day-scale flux variations and clear correlation between TeV and X-ray fluxes of Mrk 421 (Albert et al. 2007). Fossati et al. (2008) claimed a possible lag (~ 2 ks) of TeV flares relative to soft X-ray flares, whereas TeV and hard X fluxes are well correlated (see also Acciari et al. 2011).

Spectral evolutions obtained with *Suzaku* (Ushio et al. 2009) indicate that the spectral peak energy shifts to a higher energy with increasing flux in X-ray flares of Mrk 421. Another

interpretation Ushio et al. (2009) claimed is that two components, “steady” and “variable” components, coexist in X-ray flares. The “variable” component is described by a broken power-law, while the “steady” component has an exponential cutoff at ~ 1 keV. In this section, based on the picture of the “steady” and “variable” components, we argue the spectral evolution in flares in Mrk 421. As shown in Tramacere et al. (2009), the flare spectra may provide signature of the Fermi-II acceleration. Note that we do not intend to fit individual flare spectra². We just probe the qualitative behaviors of the flare spectra with our time-dependent code.

In our steady flow approximation, the identical shells are continuously ejected from $R = R_0$ as shown in Figure 1. In order to simulate flares in Mrk 421, we replace one shell in the sequence of the shells with a shell that has a different parameter set from the other shells. Then, the time-dependent contribution from the replaced shell will raise a flare on the steady emission due to the other shells. In this section, the model for the steady emission is the same as the model with the external photons in §4.2.

5.1. Variable plasma parameters

First, we propose a model in which the replaced shell has a larger diffusion coefficient and lower magnetic field than those for the other shells. The other parameters are the same as those for the other shells except for \dot{N}'_e . The magnetic field is taken as $B_0 = 0.06$ G, and K_0 is 1.5 times the value for the other shells. To harden the electron/photon spectrum of the flare, the injection rate is also changed as $\dot{N}'_e = \dot{N}_0(R/R_0)^5$ (remember $\dot{N}'_e \propto R^7$ for the other shells), where $\dot{N}_0 = 4.9 \times 10^{44} \text{ s}^{-1}$, 5 times larger than the steady model. Since the highest energy electrons are dominated by those injected earlier, we expect that emission from high energy electrons will show a large change, while emissions from low energy electrons will be unaffected.

Figure 10 shows the spectral evolution for this model. The larger K_0 shifts the peak energy of the synchrotron component to a higher energy. This is similar to the observed hardening in hard X-ray bands. This model yields a significant TeV flare as well. When we do not change the magnetic field and \dot{N}_0 (K_0 is changed as explained), a significant TeV flare does not appear (see dashed line in Figure 10). This is because of the Klein-Nishina effect. Even if the maximum energy of electrons is increased by the larger K_0 , the efficiency of the IC emission for such high-energy electrons is very low. Such electrons cool radiatively

² The minimum variability timescale in observations is also shorter than that we calculated here. But our one is within the distribution of the flare timescale.

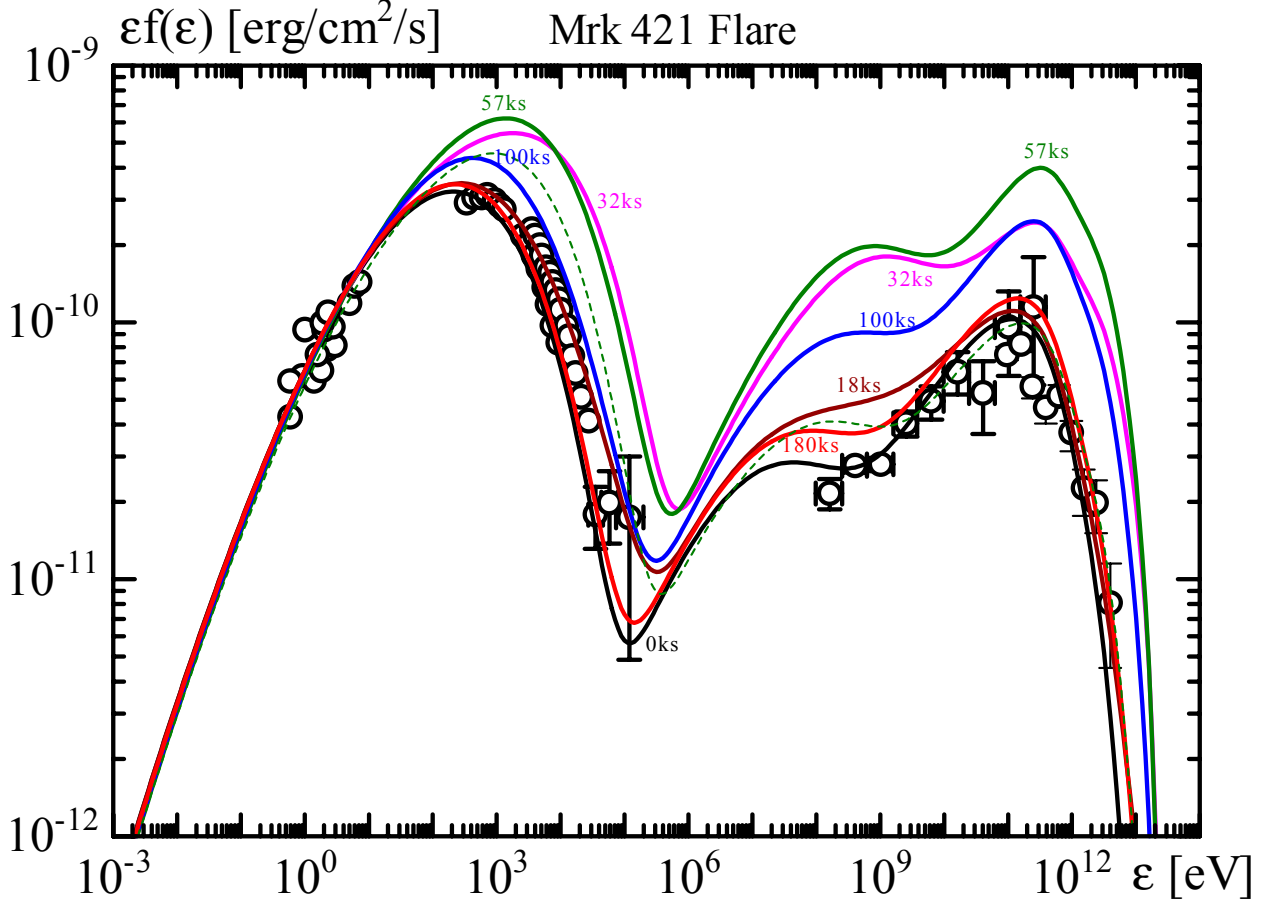


Fig. 10.— Flare from a high K' (1.5 times) and low magnetic-field ($B_0 = 0.06$ G and $\dot{N}_0 = 4.9 \times 10^{44} \text{ s}^{-1}$) shell for Mrk 421 (see §5.1). The time (ks) for observers at earth is denoted for each line. The dashed line is the spectrum at 57 ks for the model with the same magnetic field ($B_0 = 0.13$ G and $\dot{N}_0 = 9.8 \times 10^{43} \text{ s}^{-1}$) as that in the other shells.

via only synchrotron emission practically. Therefore, to synchronize a TeV flare with a X-ray flare, we need not only higher K_0 but also lower B_0 , which enhances the IC emission efficiency. Since the external photon field is common for all the shells in this model, the TeV flare inevitably accompanies a GeV flare, which is more prominent than the TeV flare. Short time flaring behavior in GeV band for Mrk421 has not been detected up to now, probably because BL Lac objects are relatively weak GeV emitters. Future examinations are valuable to support or reject EIC scenario of the GeV emission.

The required anti-correlation in B_0 and K_0 may seem awkward. As shown in eq. (5), $D \propto \varepsilon_e k |\delta B^2|_k / B \propto |\delta B^2|_k \propto \delta B_0^2 B^{-q} \varepsilon_e^q$, where δB_0^2 is the normalization coefficient of $|\delta B^2|_k$. Thus, if the decrease of B does not accompany the change of δB_0^2 , the diffusion

coefficient can be enhanced, because the resonant wavenumber k shifts lower as B decreases. However, if $\bar{\xi}$ is determined by the Alfvén velocity, $K \propto B^2 |\delta B^2|_k \propto \delta B_0^2 B^{2-q}$. Since $q < 2$, an anti-correlation in B and δB_0^2 is required to enhance the diffusion coefficient.

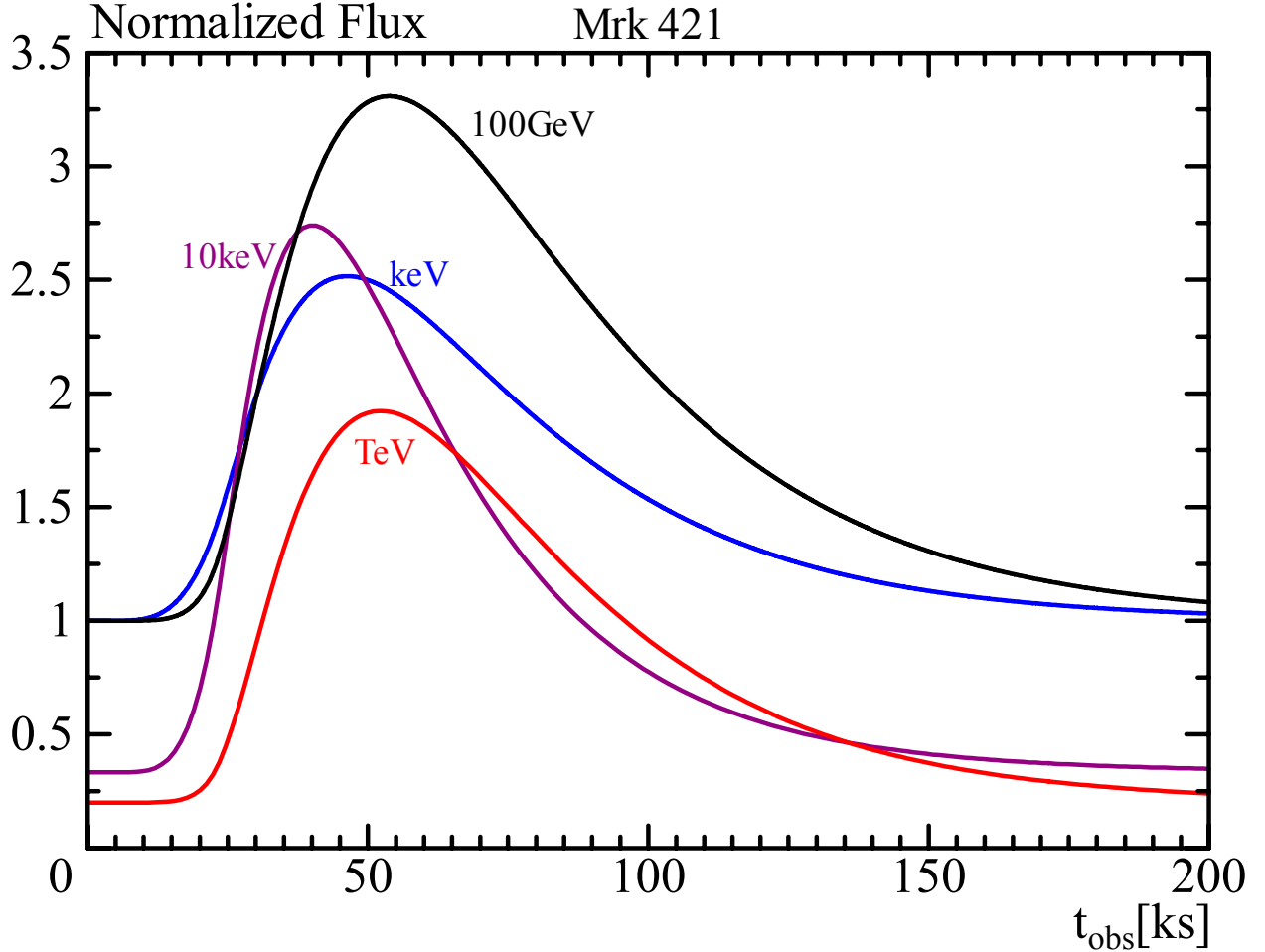


Fig. 11.— Lightcurves for Fig. 10.

As we have mentioned before, the flare in the hard X-ray band is emitted by the highest-energy electrons, while the origin of the TeV flare is SSC emissions by relatively lower-energy electrons. Because radiative cooling is very effective for the highest-energy electrons, the hard X-ray flare ceases faster than flares in other energy bands, as shown in Figure 11. This tendency is not consistent with the observed synchronicity of hard X-ray and TeV flares, or the hard lag between X-ray bands. The time-dependent simulations by Chen et al. (2011) also failed to reproduce this observed feature. The slight lag of 100 GeV–TeV lightcurves relative to the soft X-ray flare seem to be reproduced by our simulations. The model lightcurves show long tails, while typical lightcurves from blazars are almost symmetric in their rise

and decay shape. This long tail is not due to the curvature effect, namely contribution of the off-axis emission. Since the radiative cooling is inefficient for most of electrons, the decay of the flares is regulated by adiabatic cooling. Unless sudden shutdown of the emissions is artificially adopted, emissions from slowly cooling electrons yields long tails in their lightcurves.

The above two problems, the early termination of the hard X-ray flare and asymmetric lightcurves, are inevitable in our model. We have replaced only one shell changing the physical parameters to produce a flare. This implies that a partial and discrete transition of the physical parameters occurs in the outflow. Realistic outflows may have a gradual parameter change in a wider spatial range. The symmetric lightcurve may be a result of this gradual parameter change. Moreover, if the onset of the magnetic field decay is faster than the increase of the diffusion coefficient, the observed delay of hard X-ray flares should be reproduced. Thus, the hard X-ray delay requires different evolutions of the magnetic field and electron injection.

5.2. Variable Lorentz factor

A fluctuation of the bulk Lorentz factor may cause a flare as well. Shifts of the spectral peak energies are naturally expected for a photon source with a higher Γ . Strictly speaking, we cannot embed a faster shell in a steady flow of a constant Γ . Such a shell interacts with the precedent shell, and may be decelerated by shocks. Actual outflows may not be completely continuous. Hence, postulating a quasi steady outflow as a background, we simply add the contribution of the faster shell to the emission discussed in §4 here.

Given a synchrotron luminosity, a higher Γ leads to a lower synchrotron photon density in the shell frame. In order to produce simultaneous X- and TeV flares, a weaker magnetic field is required even in this case. This means that a larger K' is also required to shift the spectral peaks higher. Here, a shell with $\Gamma = 30$ is assumed as the origin of the flare. We adopt the same R_0 as before, but the high Γ leads to a narrower width $W' = 5 \times 10^{15}$ cm. Other parameters are $\Delta T'_{\text{inj}} = 2W'/c$, $B_0 = 0.03$ G, $K' = K_0(R/R_0)^{-1}$ with $K_0 = 3.9 \times 10^{-2} \text{ eV}^{1/3} \text{ s}^{-1}$, $\dot{N}'_e = \dot{N}_0(R/R_0)^5$ with $\dot{N}_0 = 4.9 \times 10^{44} \text{ s}^{-1}$.

The obtained spectra are plotted in Figure 12. If we neglect the EIC emission in this model, flares are seen in only X-ray and TeV energy bands (solid lines). However, a single outflow model with the external photons imposes the EIC emission on the flare source. The higher Γ enhances the efficiency of the EIC; given the electron total number and energy distribution in the shell frame, the EIC luminosity is proportional to Γ^6 (the Doppler factor

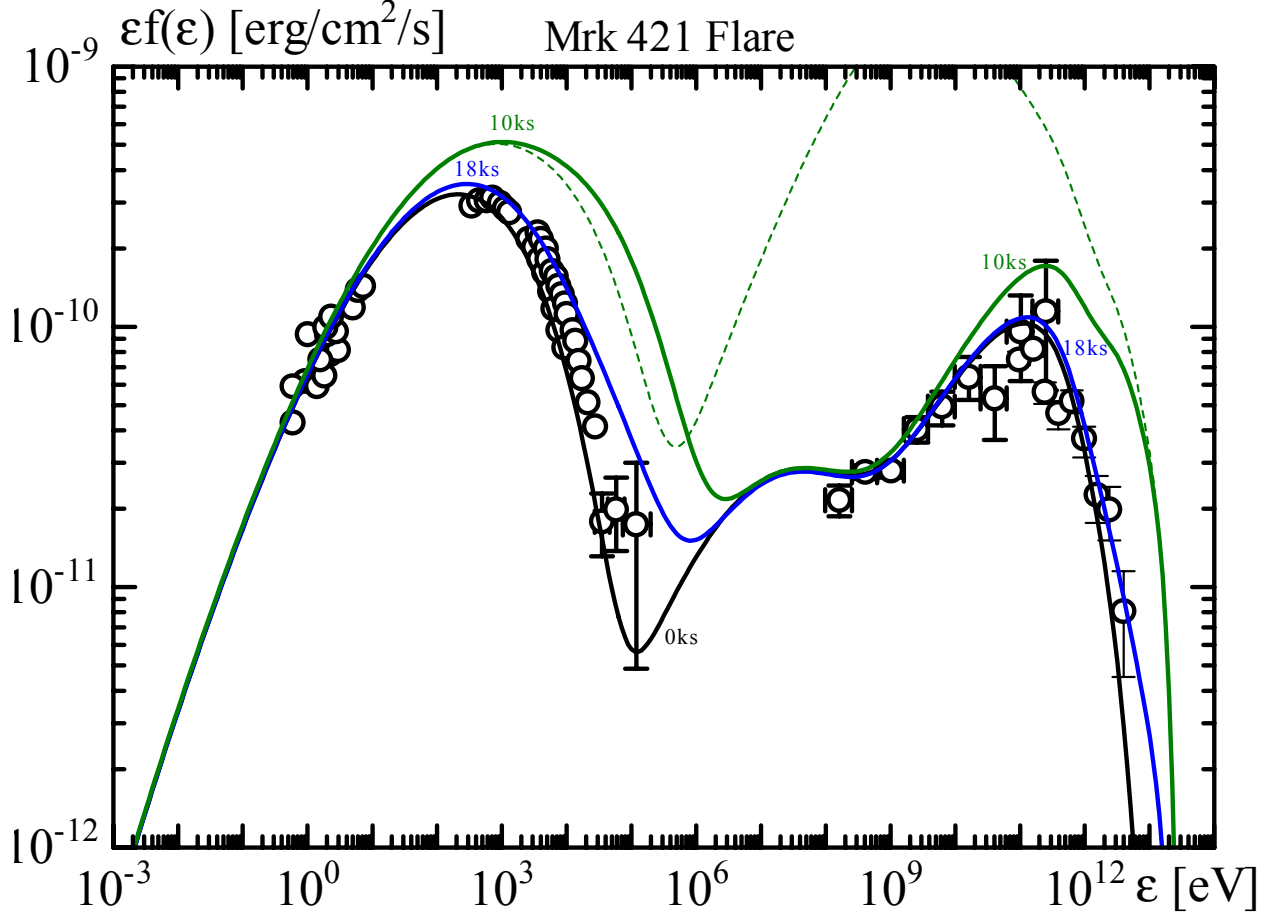


Fig. 12.— Flare from a high- Γ ($\Gamma = 30$) shell for Mrk 421 (see §5.2). The time (ks) for observers at earth is denoted for each line. The solid lines are model spectra neglecting the EIC emission. The dashed line is the spectrum at 10 ks for the model including the EIC effect.

$\delta \sim \Gamma$ is assumed), while the synchrotron luminosity $\propto \Gamma^4$ (see e.g., Dermer & Schlickeiser 2002). Hence, the amplification of the GeV flare due to the EIC emission is very large (dashed line in Figure 12). If this huge GeV flare is not observationally favorable, the high- Γ model with the external photons will be rejected. In this case, Γ should be almost constant, or a different source for the GeV steady emission (no external radio source) may be required.

When shells with different values of Γ are injected, they collide and particles are accelerated by first- and second-order Fermi processes. Böttcher & Dermer (2010) elaborated on the emission properties from such collisions and showed that the various types of the evolution of the emission spectrum are induced by such collisions. Such effects we have neglected in EIC models may be observationally constrained from the great sensitivity on Γ . This

should be tested in future studies.

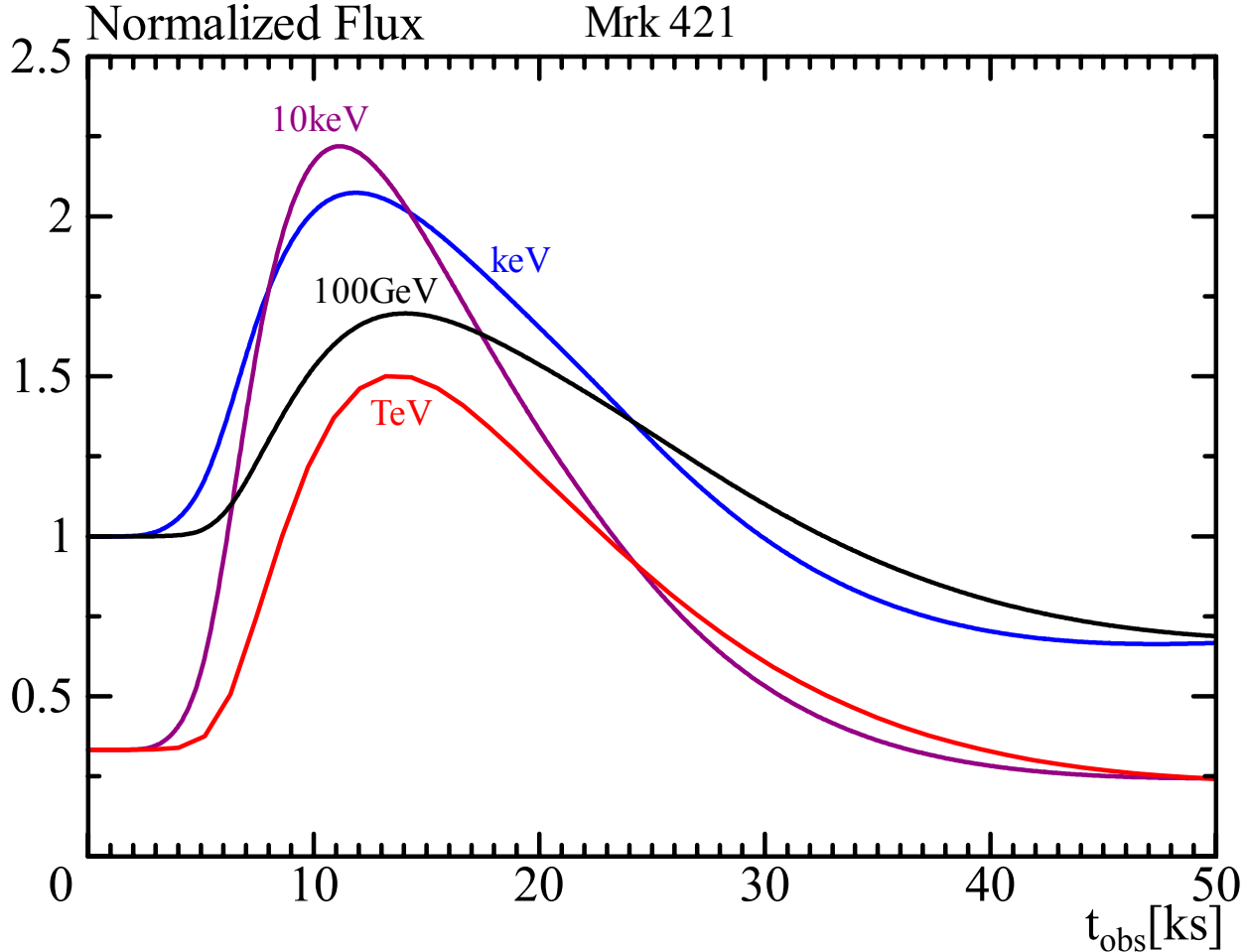


Fig. 13.— Lightcurves for Fig. 12.

The lightcurves for the model without the EIC emission are plotted in Figure 13. The high Γ leads to a short variability timescale ($\propto \Gamma^{-2}$) compared to the model in §5.1. The qualitative behaviors are similar to the case in Figure 11. The very weak magnetic field extends the cooling time scale for the highest-energy electrons. Thus, the early termination of the hard X-ray flare is not prominent compared to the model in §5.1.

5.3. Shock acceleration

While the quasi-steady emission may be due to the Fermi-II acceleration, the flare phenomena may be attributed to shocks in the outflow. The interpretation in Ushio et al.

(2009) is compatible with such a picture. As a model with a combination of Fermi-I and -II processes, Weidinger & Spanier (2010a,b) calculated electron and photon spectra, dividing the blazar region into the acceleration and radiation zones. The accelerated electrons escape from the acceleration zone and are injected into the radiation zone. By changing the particle injection, they obtained the light curves for 1ES 1218+30.4 and PKS 2155-034.

Within our picture, we also test the Fermi-I model with our code. We inject shock-accelerated electrons of the single power-law with an exponential cutoff into the flaring shell. The power-law index is $p = 2$ and the cutoff Lorentz factor is $\gamma_{e,\max} = 10^7$. The minimum Lorentz factor is taken as $\gamma_{e,\min} = 15$. The bulk Lorentz factor $\Gamma = 15$ and the shell width $W' = 1.0 \times 10^{16}$ cm are the same as those in the steady component. The injection is assumed to be constant in a time scale $\Delta T'_{\text{inj}} = W'/c$, and we neglect the reacceleration by turbulences. The total energy of electrons is $E_{e,\text{iso}} = 5 \times 10^{51}$ erg in spherically symmetric evaluation ($E_e = E_{e,\text{iso}}\theta_j^2/2 = 1.1 \times 10^{49}$ erg). Even in this model, a weak magnetic field is required as $B_0 = 0.06$ G to produce a TeV flare (see dashed line in Figure 14 for the model with $B_0 = 0.13$ G, and $E_{e,\text{iso}} = 2 \times 10^{51}$ erg).

As shown in Figure 14, the synchrotron spectra show flat shapes (photon index is ~ 2) in X-ray band. Those are significantly different from the other models. The lightcurves in Figure 15 show coincident peaks at ~ 20 ks from keV to 100 GeV. This is due to the continuous injection of the high-energy electrons. The electron injection and cooling balance each other in the high energy regions, so the electron energy distribution remains quasi-steady until the electron injection stops. The termination times of the emissions are controlled by the electron injection. The slight delay of the TeV lightcurve may come from the evolution of the seed X-ray photons.

6. Summary and Discussion

In this paper we have simulated temporal evolutions of high-energy electrons and photon production in relativistically outflowing shells. Our numerical code can follow the electron distribution with the effects of the electron injection, acceleration, synchrotron cooling, and IC cooling. The full non-linearities of IC-cooling including the Klein-Nishina effect are taken into account. We have considered the Fermi-II process as the electron acceleration mechanism, while there are other candidates of the acceleration mechanism like Fermi-I. The Fermi-II process driven by some kind of turbulences in the outflows can naturally make electron spectra harder than those predicted by the simplest version of diffusive shock acceleration theory. Differently from the shock acceleration in supernova remnants, the maximum energy of electrons is expected to be far below that in the Bohm limit. Those characteristics are

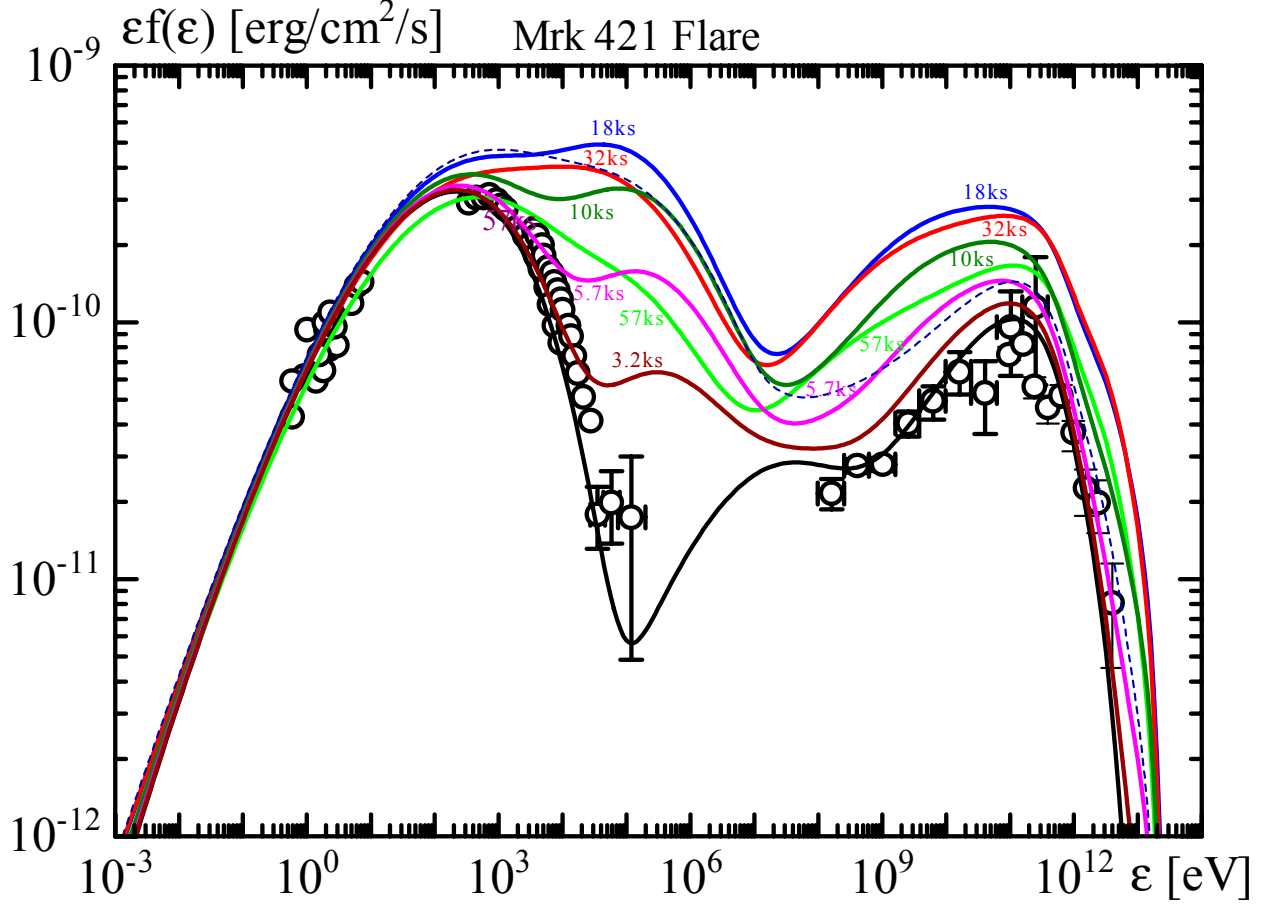


Fig. 14.— Flare from a shocked shell for Mrk 421 (see §5.3). The time (ks) for observers at earth is denoted for each line. The solid lines are model spectra with $B_0 = 0.06$ G and $E_{e,iso} = 5 \times 10^{51}$ erg. The dashed line is the spectrum at 18 ks for the model with $B_0 = 0.13$ G and $E_{e,iso} = 2 \times 10^{51}$ erg.

favorable to explain blazar photon spectra. In this method and model, the diversity in the temporal evolutions of the electron injection and acceleration can be expected to generate a variety in the photon spectral shape.

We have modeled steady photon emissions by superposition of time-evolving emissions from continuously-ejected multiple shells. The photon spectrum of the TeV blazar 1ES 1101-232 is well reproduced by a simple model with a constant injection rate and diffusion coefficient. For Mrk 421, which shows a softer spectrum than that in 1ES 1101-232, we need to adjust the evolutions of the electron injection rate etc. to fit the spectrum. A power-law evolution of $\dot{N}'_e \propto R^7$ makes a curved electron spectrum, which brings about a good fit to the observed synchrotron spectrum from radio to X-ray bands. An advantage in our model is

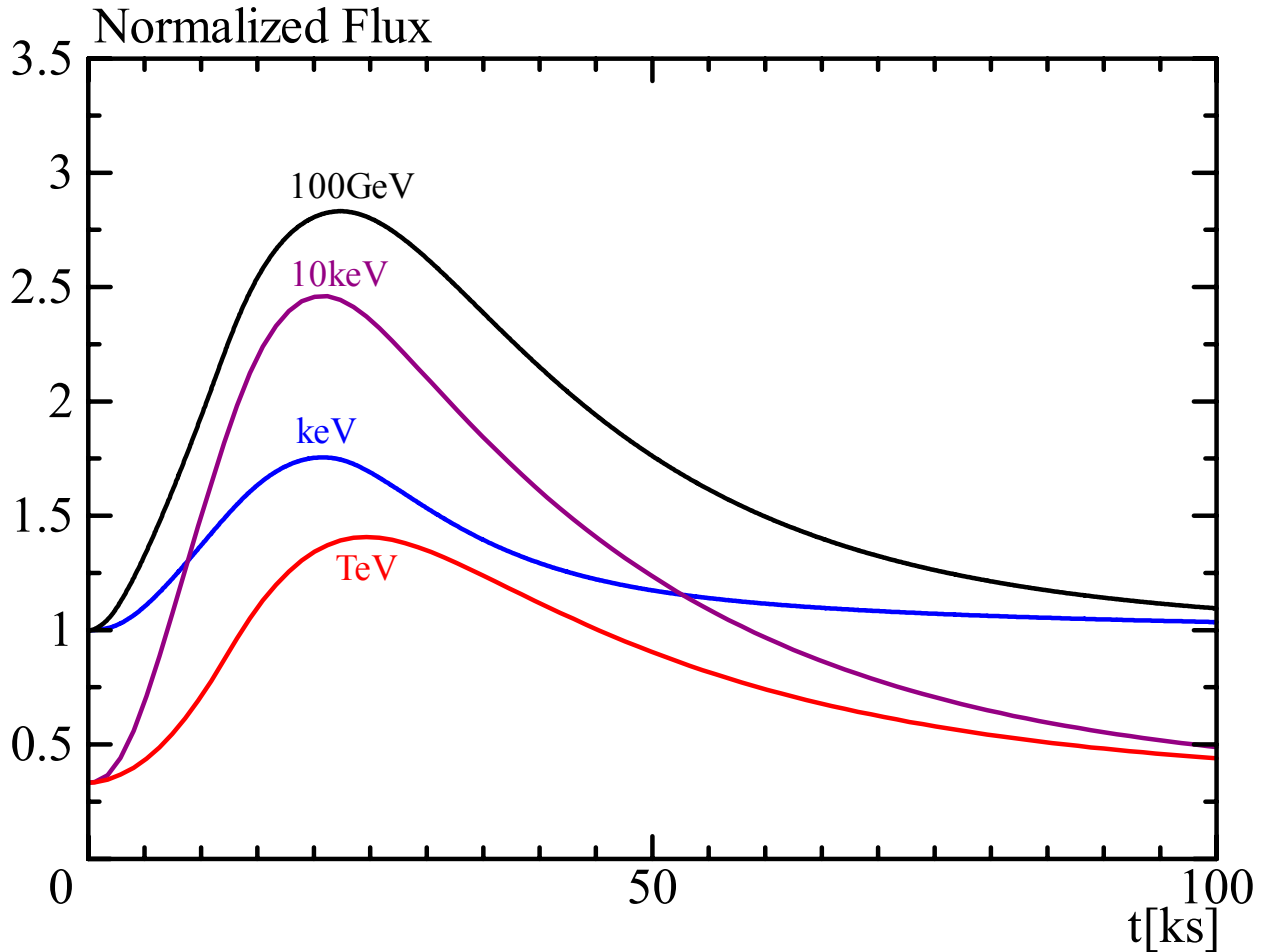


Fig. 15.— Lightcurve for Fig. 14.

that we do not need to introduce unprescribed energy scales as break energies in the electron spectrum. However, the required rapid growth of the injection rate has not been theoretically justified yet. Future progress in the study of the injection processes with time-dependent ways is desired to examine the validity of the model.

Our Fermi-II model explains the radio data as well as optical and X-ray data as the emission from a single source. In most of preceding models based on shock acceleration, which fit the optical and X-ray data of blazars, the electron density in low energy range is much higher than our model (see Figure 7), so that the synchrotron self-absorption effect is much stronger. As a result, the radio data are difficult to explain simultaneously with the optical and X-ray data by one-zone shock acceleration models, and they are frequently explained by the superposition of multi-zone self-absorbed emissions (e.g. Königl 1981). The picture we proposed is different from such models.

In this paper we have conservatively assumed the Kolmogorov type of turbulences, $q = 5/3$. An alternative way to make a soft electron spectrum is adopting a larger value of q . Even if \dot{N}'_e and K' are constant, the hard-sphere scattering ($q = 2$, see e.g. Park & Petrosian 1995) leads to a soft electron spectrum as shown in Figure 2. This case implies that the acceleration timescale is independent of the particle energy, which is similar to the original idea of Fermi (1949). Another possibility is the effect of the particle escape (e.g. Becker, Le & Dermer 2006), while we have not included this effect. Especially for the model with $q = 2$, the escape timescale is independent of the particle energy so that the effect can be prominent. The escape effect will not only change the spectral index of the electron distribution, in some cases but also may introduce cutoffs in N_e . We may need at least two zones, acceleration region and emission region, to simulate such models without neglecting the contribution of the escaped particles. Note that the model of Weidinger & Spanier (2010a,b) is the two-zone one. However, the accelerated electrons are injected in the emission zone uniformly and the effect of geometrical separation of the acceleration and emission zones are not considered.

It is interesting that the obtained electron spectrum is close to the log-parabolic function in the most important energy range. In Massaro et al. (2004a) the origin of this shape is attributed to the energy dependence of the escape probability. However, our time-dependent calculations have not included the escape effect. The analytical study of the Fermi-II process by Park & Petrosian (1995) based on Green's functions may be a meaningful hint for this spectral shape. Since most high energy electrons are injected at early times, their spectral shape primarily determined by the Green function for a single injected energy. The spectral shapes around the synchrotron peak predicted by the DBP and log-parabolic models are hard to be distinguished from our model. Thus, to search for the signature of the electron minimum energy required in those analytical models, future infrared and submillimeter observations are interesting.

In order to reproduce the GeV flux for Mrk 421 by our single emission-region model, an external radio photon field is needed. The radio photons interacting with high-energy electrons in the outflow can be up-scattered to GeV energies. The required radio luminosity $4.9 \times 10^{38} \text{ erg s}^{-1}$ is far below the bolometric luminosity $1.4 \times 10^{43} \text{ erg s}^{-1}$ (assuming $\theta_j = 1/15$). Alternatively, an additional emission region may contribute as a GeV photon source. Correlation analyses of flux variabilities between GeV and another band may provide a clue to the GeV emission region. While significant variability (factor of about three) of GeV flux has been reported (Abdo et al. 2011), the correlations with X or TeV variabilities seem still ambiguous to determine the model.

By replacing a shell in the sequence of the identical shells, and changing the parameters, we simulate flare phenomena. In this method, the flare lightcurves show asymmetric

shapes. The flare emissions gradually fade out via adiabatic cooling. To reproduce the symmetric lightcurves as frequently seen in blazar flares, gradual changes of the parameters may be required, while our models correspond to discrete changes of the parameters. The cooling time of the electrons that emit hard X-rays is quite short. Therefore, a gradual cease of the electron injection or acceleration in this highest energy range may be required to synchronize the peak times of the hard X-ray and TeV lightcurves. A sudden shut down of acceleration/injection would lead to an early hard X-ray termination. The most critical thing to produce simultaneous flares in X-ray and TeV bands is decrease of the magnetic field. The Klein-Nishina effect prevents TeV flare caused by a growth of the diffusion coefficient that increases the electron maximum energy. An enhancement of the SSC emission efficiency by weakening the magnetic field is required to generate a TeV flare. The required anti-correlation between the fluxes and magnetic field is a challenging problem.

For the EIC model, high variability of the bulk Lorentz factor Γ is not favorable. Since the EIC emission is sensitive to Γ , the observed GeV variability, by a factor of about three, strictly constrains the fluctuation of Γ .

First we appreciate the anonymous referee for valuable comments to improve our paper significantly. This study is partially supported by Grants-in-Aid for Scientific Research No.25400227 and 24540258 from the Ministry of Education, Culture, Sports, Science and Technology (MEXT) of Japan (KA), and JSPS Research Fellowships for Young Scientists No.231446 (KT).

REFERENCES

- Abdo, A. A. et al., 2011, *ApJ*, 736, 131
- Acciari, V. A. et al., 2011, *ApJ*, 738, 25
- Agudo, I. et al., 2001, *ApJ*, 549, L183
- Aharonian, F. A., & Atoyan, A. M. 1999, *A&A*, 351, 330
- Aharonian, F. et al., 2006, *Nature*, 440, 1018
- Aharonian, F. et al., 2007, *A&A*, 470, 475
- Aharonian, F., Akhperjanian, A. G., Barres de Almeida, U., et al. 2007a, *A&A*, 475, L9
- Albert, J. et al., 2007, *ApJ*, 663, 125

- Asano, K., & Mészáros, P. 2011, *ApJ*, 739, 103
- Asano, K., & Mészáros, P. 2012, *ApJ*, 757, 115
- Asano, K., & Terasawa, T. 2009, *ApJ*, 705, 1714
- Band, D. et al. 1993, *ApJ*, 413, 281
- Becker, P. A., Le, T., & Dermer, C. D. 2006, *ApJ*, 647, 539
- Blandford, R., & Eichler, D. 1987, *PhR*, 154, 1
- Böttcher, M., & Dermer, C. D. 2010, *ApJ*, 711, 445
- Böttcher, M., Pohl, M., & Schlickeiser, R. 1999, *Astropart. Phys.*, 10, 47
- Celotti, A., & Ghisellini, G. 2008, *MNRAS*, 385, 283
- Chen, X. et al. 2011, *MNRAS*, 416, 2368
- Daly, R. A., & Marscher, A. P. 1988, *ApJ*, 334, 539
- Dermer, C. D., & Schlickeiser, R. 2002, *ApJ*, 575, 667
- Dung, R., & Schlickeiser, R. 1990, *A&A*, 240, 537
- Fermi, E., 1949, *Phys. Rev.*, 75, 1169
- Fossati, G. et al., 2008, *ApJ*, 677, 906
- Ghisellini, G., Tavecchio, F., and Chiaberge, M. 2005, *A&A*, 432, 401
- Hardee, P. E. 2004, *Ap&SS*, 293, 117
- Inoue, S., & Takahara, F. 2002, *ApJ*, 463, 555
- Katarzyński, K., Ghisellini, G., Mastichiadis, A., Tavecchio, F., & Maraschi, L. 2006, *A&A*, 453, 47
- Kino, M., Takahara, F., & Kusunose, M. 2002, *ApJ*, 564, 97
- Kirk, J. G., Rieger, F. M., & Mastichiadis, A. 1998, *A&A*, 333, 452
- Kneiske, T. M., Bretz, T., Mannheim, K., & Hartmann, D. H. 2004, *A&A*, 413, 807
- Komissarov, S. S., & Falle, S. A. E. G. 1997, *MNRAS*, 288, 833

- Königl, A. 1981, *ApJ*, 243, 700
- Kusunose, M., Takahara, F., & Li, H. 2000, *ApJ*, 536, 299
- Lefa, E., Rieger, F. M., & Aharonian, F. 2011, *ApJ*, 740, 64
- Lyubarskii, Y. E. 1999, *MNRAS*, 308, 1006
- Malkov, M. A., & Drury, L. O’C. 2001, *Rep. Prog. Phys.*, 64, 429
- Massaro, E., Perri, M., Giommi, P., & Nesci, R. 2004, *A&A*, 413, 489
- Massaro, E., Perri, M., Giommi, P., Nesci, R., & Verrecchia, F. 2004, *A&A*, 422, 103
- Mészáros, P. 2006, *Rep. Prog. Phys.*, 69, 2259
- Mizuno, Y., Hardee, P. E., & Nishikawa, K. 2007, *ApJ*, 662, 835
- Mizuno, Y., Hardee, P. E., & Nishikawa, K. 2011, *ApJ*, 734, 19
- Narayan, R., Li, J., & Tchekhovskoy, A. 2009, *ApJ*, 697, 1681
- Neronov, A., & Vovk, I. 2010, *Science*, 328, 73
- Park, B., & Petrosian, V. 1995, *ApJ*, 446, 699
- Rybicki, G. B., & Lightman, A. P. 1979, *Radiative Processes in Astrophysics* (New York: Wiley-Interscience)
- Schlickeiser, R. 1984, *A&A*, 136, 227
- Schlickeiser, R. 1985, *A&A*, 143, 431
- Schlickeiser, R., Campeanu, A., & Lerche, L. 1993, *A&A*, 274, 614
- Schlickeiser, R., & Dermer, C. D. 2000, *A&A*, 360, 789
- Snellen, I. A. G., Mack, K.-H., Schilizzi, R. T., & Tschager, W. 2004, *MNRAS*, 348, 227
- Spada, M., Ghisellini, G., Lazzati, D., & Celotti, A. 2001, *MNRAS*, 325, 1559
- Stawarz, L., & Petrosian, V. 2008, *ApJ*, 681, 1725
- Tramacere, A. et al., 2009, *A&A*, 501, 879
- Ushio, M. et al., 2009, *ApJ*, 699, 1964

Vainio, R., & Schlickeiser, R. 1999, *A&A*, 343, 303

Vainio, R., Virtanen, J. J. P., & Schlickeiser, R. 2003, *A&A*, 409, 821, Erratum: 2005, *A&A*, 421, 7

van Leer, B. 1979, *J. Comput. Phys.*, 32, 101

Weidinger, M. & Spanier, F. 2010a, *A&A*, 515, A18

Weidinger, M. & Spanier, F. 2010b, *Int. J. Mod. Phys. D*, 19, 887

Yamazaki, R., Yoshida, T., Terasawa, T., Bamba, A., & Koyama, K. 2004, *A&A*, 416, 595

Zacharias, M., & Schlickeiser, R. 2012, *ApJ*, 761, 110